Proposal to PAC 53

Double Deeply Virtual Compton Scattering with the SoLIDμ spectrometer

Xinzhan Bai*, Alexandre Camsonne*†, Kondo Gnanvo

Thomas Jefferson National Accelerator Facility
12000 Jefferson Avenue, Newport News, Virginia 23606, USA

Juan-Sebastian Alvarado*, Raphaël Dupré, Adam Hobart, Dominique Marchand, Carlos Muñoz Camacho, Silvia Niccolai, Eric Voutier*

Université Paris-Saclay, CNRS/IN2P3/IJCLab
15 rue Georges Clémenceau, 91406 Orsay, France

Haiyan Gao, Yining Liu, Bo Yu, Yi Yu, Zhiwen Zhao*, Jingyi Zhou

Duke University, Durham, NC 27708

Debaditya Biswas, Marie Boër*, Gyang Chung, Mahmoud Gomina

Virginia Polytechnic Institute and State University, Blacksburg, VA 24061

Ronald Gilman

Rutgers University Rutgers, The State University of New Jersey
136 Frelinghuysen Road Piscataway, NJ 08854-8019

Nilanga Linayage

University of Virginia
Charlottesville, VA 22904-4714

Yi Wang, Junhuai Xu, Zhihong Ye, Haojie Zhang, Yaopeng Zhang

Tsinghua University, Beijing 100084, China

Evaristo Cisbani

Istituto Superiore di Sanità
299 Viale Regina Elena, Roma 00161, Italia

Guido Maria Urcioli

INFN, Sezione di Roma1
2 Piazzale Aldo Moro, Roma 00185, Italia

Vincenzo Bellini, Concetta Maria Sutera

Dipartimento di Fisica a Astronomica, Università di Catania,
64 Via S. Sofia, Catania 95123, Italia

Anthony W. Thomas

ARC Special Research Centre for the Subatomic Structure of Matter (CSSM)
University of Adelaïde, School of Chemistry and Physics, Adelaïde SA 5005, Australia

Pierre Chatagnon[#], Maxime Defurne[#], Víctor Martínez-Fernández[#, ‡], Hervé Moutarde[#], Franck Sabatié[#]

[#] *IRFU, CEA, Université Paris-Saclay, F-91191 Gif-sur-Yvette, France*
[‡] *Center for Frontiers in Nuclear Science, Stony Brook University, Stony Brook, NY 11794, USA*

Malek Mazouz

Faculté des Sciences de Monastir, Département de Physique
Monastir 5000, Tunisia

Whitney Armstrong, Sylvester Joosten, Zein-Eddine Meziani

Argonne National Laboratory, Physics Division
Bdg. 203, 9700 S. Cass Avenue, Argonne IL 60439, USA

Thomas Hemmick

Stony Brook University, Department of Physics and Astronomy
C-107/S-200 Physics Building, Stony Brook NY 11794-3800, USA

Bernard Pire

Centre de Physique Théorique, CNRS, École polytechnique, I.P. Paris
91128 Palaiseau, France

P. Sznajder, and J. Wagner

National Centre for Nuclear Research, NCBJ, 02-093 Warsaw, Poland

and the Hall A SoLID collaboration

Proposal as of April 22, 2025

[†] Contact person
[*] Spokesperson

Executive Summary

This proposal, which follows the previous Letter-of-Intent LOI12-15-005, aims at the measurement of the Double Deeply Virtual Compton Scattering (DDVCS) process in the di-muon channel ($e^- p \to e^- p \gamma^* \to e^- p \mu^+ \mu^-$) with the SoLID spectrometer supplemented with a forward angle muon detector.

The Compton scattering of a virtual photon in the deep inelastic regime, or so-called DDVCS, constitutes a unique access to generalized parton distributions (GPDs). The virtuality of the final photon enables the decorrelated investigation of the x- and ξ-dependences (respectively, longitudinal momentum fraction and skewness) of GPDs, as opposed to Deeply Virtual Compton Scattering and Timelike Compton scattering which access (at leading order in α_s) GPDs along the diagonals $x{=}\pm\xi$. The main physics goal of the proposed experiment is to determine Compton Form Factors (CFFs) and Generalized Parton Distributions (GPDs) in the region $x < |\xi|$. Such measurements are of relevance not only for the precise knowledge of GPDs but most importantly for the understanding of the nucleon structure properties. This includes nucleon tomography through transverse momentum parton densities which rely on the extrapolation of the Fourier transform of GPDs in the limit $\xi \to 0$, and the distribution of spin and forces in the nucleon through the gravitational form factors.

The golden observable of the proposed measurements is the Beam Spin Asymmetry (BSA) which accesses the imaginary part of Compton Form Factors (CFFs), that is the GPD value at a given point of the physics phase-space. Similarly to Deeply Virtual Compton Scattering (DVCS) and Timelike Compton Scattering (TCS), this observable is obtained from the comparison of the number of experimental events measured for opposite beam helicities. Differently from DVCS and TCS and because of the smallness of the cross section, the event distributions are preliminary integrated over the muon-pair polar angle and either the muon-pair (DVCS-like observable) or the final virtual photon (TCS-like observable) azimuthal angle. Additionally, the helicity independent distributions of experimental events allow us to access the real part of CFFs through the muon charge asymmetry, that is the comparison of the number of experimental events obtained for muons of opposite charge at the same point of the physics phase-space.

The experiment is proposed to run over 100 days with a 11 GeV polarized electron beam, half of it in parallel with the approved SoLID J/ψ experiment (E12-12-006). Similarly, it will use a 3 μA beam intensity however highly polarized (>85%), a 15 cm liquid hydrogen target, and the SoLID spectrometer. The SoLID detector system will be complemented at forward angles with muon detection capabilities, constituting overall the SoLIDμ spectrometer. It will deliver a significant set of experimental data about di-muon production at different deep inelastic regimes, and will bring novel observables of GPD physics at $x < |\xi|$. At the same time, this will expand the J/ψ and TCS experiment to the di-muon channel from the approved di-electron channel.

Contents

1 Introduction

The concept of Generalized Parton Distributions (GPDs) [1] profoundly renewed and extended the understanding of the structure and dynamics of the nucleon [2, 3]. They parameterize the nucleon structure in terms of matrix elements describing the correlations between the transverse position of quarks and gluons and their longitudinal momentum [4, 5]. GPDs so access the internal dynamics of the nucleon as expressed by the Ji sum rule linking GPDs to the angular momentum [6], and the second moment of GPDs giving insights about the distribution of nuclear forces [7]. The first moment of GPDs reduces to the nucleon form factors, while they take the form of parton distributions in their forward limit. Consequently, GPDs appear as fundamental building elements of the nuclear structure knowledge, asking for a precise and complete experimental determination.

GPDs can be accessed in the hard scattering regime of exclusive electron scattering reactions when a high-enough virtual photon (Q^2) is exchanged with a parton while the quadri-momemtun transfer t to the nucleon is small enough ($|t|/Q^2 \ll 1$). This provides the necessary scale difference to separate the probe (the perturbative hard scattering of a virtual photon) from the object (the nucleon with its non-perturbative structure), that is to factorize the reaction amplitude [8]. Beside these variables, GPDs also depend on the longitudinal momentum fraction x of the initial parton and on the transferred longitudinal momentum fraction or skewness ξ to the final parton. In the Bjorken regime ($Q^2 \gg 1$ (GeV/c^2)^2 and $t \to 0$, GPDs may be interpreted as a $1/Q$ resolution distribution in the transverse plane of partons carrying some longitudinal momentum fraction [9, 10, 11, 12].

Hard exclusive Compton-like scattering reactions are considered golden channels to access GPDs because involving only one non-perturbative structure of the nucleon, differently from meson production. These comprise: Deeply Virtual Compton Scattering (DVCS) where an initial virtual photon (Q^2) produced by a lepton beam transforms into a real photon; the reciprocal process Timelike Compton Scattering (TCS) where a real photon transforms into a timelike virtual photon (Q'^2) decaying into a lepton-pair; and the Double Deeply Virtual Compton Scattering (DDVCS) where an initial virtual photon (Q^2) scatters off a parton and creates a lepton-pair from the final timelike virtual photon (Q'^2)[1]. In that respect, DDVCS is the most general case of hard exclusive Compton-like scattering reactions which limits are TCS when Q^2=0 and DVCS when Q'^2=0. This reflects in the physics potential of each processes: while TCS and DVCS access unambiguously GPDs along the diagonals x=$\pm\xi$, DDVCS is not restricted by this condition and can access unambiguously GPDs in the so-called Efremov-Radyushkin-Brodsky-Lepage (ERBL) evolution region where $|x| \leq \xi$ [15, 16, 17]. This allows to decouple the x- and ξ-dependences opening off-diagonal investigation of GPDs. More importantly, it enables to constrain the deconvolution of these two variables and the zero-skewness extrapolation required for nucleon tomography [9].

DVCS has been experimentally investigated for the past $\sim$20 years, and first measurements of TCS from CLAS12 have recently been published [18]. The combination of cross section smallness and difficult theoretical interpretation of electron induced DDVCS when detecting the e^+e^--pair from the final virtual photon did forbid up to now any reliable experimental study[2]. Taking advantage of the energy upgrade of the CEBAF accelerator and of the development of the SoLID detection and luminosity capabilities, we propose to investigate the electroproduction of $\mu^+\mu^-$ di-muon pairs and measure the beam-spin asymmetry and the muon charge asymmetry of the exclusive $ep \to ep\gamma^* \to ep\mu^+\mu^-$ reaction in the hard scattering regime. A specific muon detector is proposed to complement the planned SoLID spectrometer and allows for the detection of di-muon pairs.

The next section reviews the main characteristics of the DDVCS process and the GPD content of the experimental observables of interest. The benefits of DDVCS measurements for the achievement of the GPD experimental program are specifically discussed in the following section, before adressing the description of the experimental setup constituting the base SoLID spectrometer and the foreseen extension SoLID$_\mu$ required for di-muon detection. Finally, the expected counting rates and experimental data are presented based on the simulation package of the SoLID$_\mu$ spectrometer and the VGG modeling [19] of the Bethe-Heitler and DDVCS cross sections.

[1] The production of a photon pair with a large invariant mass is another golden channel in that sense; see Ref. [13, 14].

[2] The e^+e^--pair final state requires antisymmetrization of the electron wave function to take into account indiscernable final electrons as well as the careful treatment of the quantum interference with the decay of the full meson excitation spectra, which in practice dilute or even cancel an eventual DDVCS signal.

2 Double deeply virtual Compton scattering

2.1 Access to Generalized Parton Distributions

Similarly as the light diffusion from a material tells about its internal structure, the light scattered by a nucleon carries information about the parton dynamics and structure, providing that the wavelength associated to this light is smaller than the nucleon size. The Compton scattering of a virtual photon with quadri-momentum $Q^2 > 1$ (GeV/c^2)^2 is capable of resolving the internal structure of the nucleon. The most general realization of the deep regime of this process is the double deeply virtual Compton scattering which representation through the handbag diagram (Fig. 1) illustrates the access to GPDs.

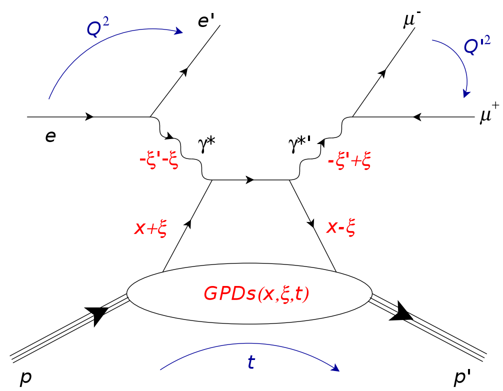

Figure 1: DDVCS handbag diagram: the initial and final virtual photon momenta are respectively q and q', and similarly for the initial and final proton momenta p and p'; Δ is the momentum transfer to the nucleon; the longitudinal momentum flow corresponds to (-)2ξ for the (partons) virtual photons.

At leading twist and leading α_s-order, the DDVCS process can be seen as the absorption of a space-like photon by a parton of the nucleon, followed by the quasi-instantaneous emission of a time-like photon by the same parton, which finally decays into a lepton/anti-lepton pair (Fig. 1). The scaling variables attached to this process are defined as

$$\xi = \frac{Q^2 + Q'^2}{2Q^2/x_{\rm B} - Q^2 - Q'^2 + t} \quad (1)$$

$$\xi' = \frac{Q^2 - Q'^2 + t/2}{2Q^2/x_{\rm B} - Q^2 - Q'^2 + t} \quad (2)$$

representing the skewness (ξ) and the Bjorken generalized variable (ξ'). If Q'^2=0, the final photon becomes real, corresponding to the DVCS process and the restriction ξ'=ξ in the Bjorken limit. If Q^2=0, the initial photon is real, referring to the TCS process and the restriction ξ'=$-\xi$ in the Bjorken limit. The DDVCS reaction amplitude is proportional to a combination of the Compton Form Factors (CFFs) $\mathcal{F}$ (with $\mathcal{F} \equiv \{\mathcal{H}, \mathcal{E}, \widetilde{\mathcal{H}}, \widetilde{\mathcal{E}}\}$) defined from the GPDs F (with $F \equiv \{H, E, \widetilde{H}, \widetilde{E}\}$) as

$$\mathcal{F}(\xi', \xi, t) = \mathcal{P} \int_{-1}^{1} F_+(x, \xi, t) \left[\frac{1}{x - \xi'} \pm \frac{1}{x + \xi'} \right] dx - i\pi F_+(\xi', \xi, t) \quad (3)$$

where $\mathcal{P}$ denotes the Cauchy's principal value integral, and

$$F_+(x, \xi, t) = \sum_q \left(\frac{e_q}{e} \right)^2 [F^q(x, \xi, t) \mp F^q(-x, \xi, t)] \quad (4)$$

is the singlet GPD combination for the quark flavor q. In these expressions, the upper sign holds for vector GPDs (H^q, E^q) and the lower sign for axial vector GPDs ($\widetilde{H}^q, \widetilde{E}^q$). In comparison to DVCS and TCS, the imaginary part of the DDVCS CFFs access the GPDs at x=$\pm\xi' \neq \xi$ instead of x=$\pm\xi$, and the real part of the DDVCS CFFs involves a convolution with different parton propagators.

Varying the virtuality of both incoming and outgoing photons changes the scaling variables ξ' and ξ and maps out the GPDs as function of its arguments independently. From Eq. 2-1, one obtains

$$\xi' = \xi \, \frac{Q^2 - Q'^2 + t/2}{Q^2 + Q'^2} \tag{5}$$

indicating that ξ', and thus the imaginary parts of the CFFs $\{\mathcal{H}, \mathcal{E}\}$, changes sign around $Q^2{=}Q'^2$. This represents a strong testing ground of the universality of the GPD formalism [20].

As a consequence of the time-like nature of the final photon, the DDVCS process is restricted to the ERBL region and GPDs can be accessed only in the domain $|x| < \xi$. Although the whole physics phase-space is not accessed, this is a tremendous gain of information since no deconvolution is involved. DDVCS so provides the necessary framework for an uncorrelated measurement of the GPDs as a function of both scaling variables x and ξ [21].

2.2 Experimental observables

DVCS has been the main focus of experimental programs for the past two decades, since factorization was shown to hold already at electron beam energies of 6 GeV [22]. Several DVCS observables have been measured: polarized an unpolarized cross section off the proton [22, 23, 24, 25, 26, 27, 28, 29] and off the neutron [30, 31], beam spin asymmeties off the proton [32, 33, 34] and more recently off the neutron [35], target spin asymmetries off longitudinally [36, 37, 38, 39] and transversely [40] polarized protons, and beam charge asymmetries [41, 42]. The first ever measurement of TCS was recently released [18] and no measurements so far of DDVCS have yet been performed. With its high luminosity and large acceptance capabilities, the SoLID spectrometer is ideally suited for the investigation of the DDVCS process.

2.2.1 Cross section

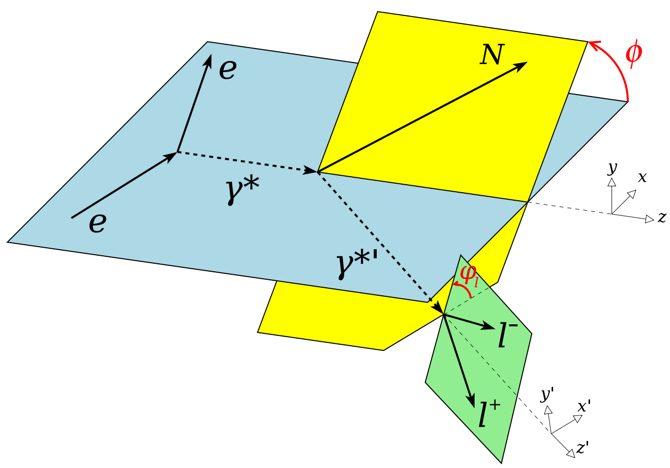

Figure 2: Reference frames of the reaction $^1\mathrm{H}(e, e'pl_+l_-)$.

Considering the $\mu^+\mu^-$-pair channel of the general di-lepton pair production (Fig. 2)

$$e(k) + p(p) \to \mathrm{e}'(k') + p'(p') + \gamma^\star(q') \to \mathrm{e}'(k') + p'(p') + \mu^+(l_+) + \mu^-(l_-)\,, \tag{6}$$

the virtualities of the photons entering the DDVCS process are defined as

$$Q^2 = -q^2 \qquad Q'^2 = q'^2 \tag{7}$$

and the four-momentum to the nucleon as

$$\Delta = p' - p = q - q' \tag{8}$$

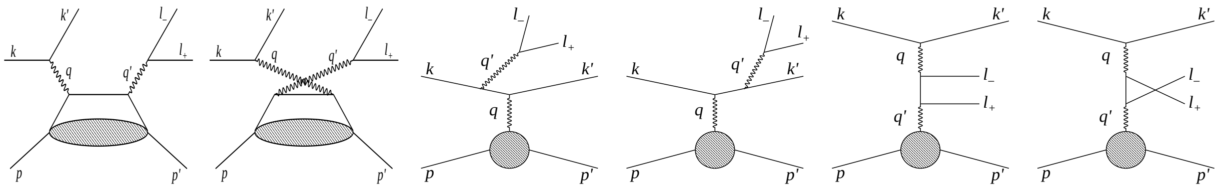

Figure 3: The different reaction amplitudes contributing to the $ep \to epl_+l_-$ cross section with, from left to right: the DDVCS direct and crossed terms, the initial and final state radiation of the Bethe-Heitler process (BH$_1$), the direct and crossed terms of the vacuum excitation (BH$_2$).

with t=Δ^2. The *average* photon and nucleon momenta are

$$\overline{q} = \frac{q+q'}{2} \qquad \overline{p} = \frac{p+p'}{2} \tag{9}$$

and the DDVCS scaling variables are accordingly [21, 17] (in [17], ξ' was denoted as ρ)

$$\xi = -\frac{1}{2}\,\frac{\Delta\cdot\overline{q}}{\overline{p}\cdot\overline{q}} \qquad \xi' = -\frac{1}{2}\,\frac{\overline{q}\cdot\overline{q}}{\overline{p}\cdot\overline{q}} \tag{10}$$

which reduces to Eq. 1 and Eq. 2 at leading twist.

The electroproduction of di-muon proceeds through the coherent sum of three elementary processes (Fig. 3): the DDVCS process where the di-muon originates from a parton, the Bethe-Heitler mechanism (BH$_1$) where the di-muon are radiated by the initial or final electron, and the di-muon production from the vacuum excitation in the vicinity of the nuclear field (BH$_2$). Correspondingly, the di-muon production cross section induced by a longitudinally polarized (λ) electron beam off an unpolarized nucleon may be written [21]

$$d^7\sigma^\lambda \equiv \frac{d^7\sigma^\lambda}{dx_B\,dy\,dt\,d\phi\,dQ'^2\,d\Omega_\mu} = \frac{1}{(2\pi)^3}\,\frac{\alpha^4}{16}\,\frac{x_B y}{Q^2\sqrt{1+\varepsilon^2}}\,\sqrt{1-\frac{4m_\mu^2}{Q'^2}}\;|\mathcal{T}^\lambda|^2, \tag{11}$$

where the reaction amplitude can generically be expressed as

$$|\mathcal{T}^\lambda|^2 = |\mathcal{T}_{DDVCS}|^2 + \mathcal{I}_1^\lambda + \mathcal{I}_2^\lambda + |\mathcal{T}_{BH_1}|^2 + |\mathcal{T}_{BH_2}|^2 + \mathcal{T}_{BH_{12}}, \tag{12}$$

featuring the pure DDVCS amplitude $|\mathcal{T}_{DDVCS}|^2$, the beam polarization sensitive interference amplitudes $\mathcal{I}_1^\lambda$ and $\mathcal{I}_2^\lambda$ between the DDVCS and BH$_i$ processes, and the pure BH amplitude built itself from the two elementary BH$_i$ processes. Following Ref. [21], the harmonic structure of the DDVCS and interference amplitudes at leading twist and leading α_S-order can be written

$$|\mathcal{T}_{DDVCS}|^2 = \frac{2\xi'^2}{Q^4y^2\tilde{y}^2(\xi^2-\xi'^2)}\sum_{n=0}^{2} c_n^{VCS}(\varphi_\mu)\cos(n\phi)\,, \tag{13}$$

$$\mathcal{I}_1^\lambda = \frac{2\xi'(1-\xi)}{Q^2\Delta^2y^3\tilde{y}^3(\xi^2-\xi'^2)}\,\frac{\tilde{y}}{P_1P_2}\sum_{n=0}^{3}\left[c_n^1(\varphi_\mu)\cos(n\phi) + \lambda\, s_n^1(\varphi_\mu)\sin(n\phi)\right]\,, \tag{14}$$

$$\mathcal{I}_2^\lambda = \frac{2\xi'(1-\xi)}{Q^2\Delta^2y^3\tilde{y}^3(\xi^2-\xi'^2)}\,\frac{y}{P_3P_4}\sum_{n=0}^{3}\left[c_n^2(\phi)\cos(n\varphi_\mu) + \lambda\, s_n^2(\phi)\sin(n\varphi_\mu)\right]\,, \tag{15}$$

with the kinematical parameters

$$y = \frac{p\cdot q}{p\cdot k} \qquad \tilde{y} = \frac{p\cdot l_-}{p\cdot q'} \tag{16}$$

and the P_i's propagators of the intermediate leptons of the BH processes

$$P_1 = -\frac{1}{2\xi}\frac{(k'+\Delta)^2}{\overline{p}\cdot\overline{q}} \quad P_2 = -\frac{1}{2\xi}\frac{(k-\Delta)^2}{\overline{p}\cdot\overline{q}} \quad P_3 = \frac{1}{2\xi}\frac{(l_++\Delta)^2}{\overline{p}\cdot\overline{q}} \quad P_4 = \frac{1}{2\xi}\frac{(l_-+\Delta)^2}{\overline{p}\cdot\overline{q}}\,. \tag{17}$$

Similarly to spacelike DVCS process, the Fourier coefficient c_n^{VCS} comprise bilinear combinations of CFFs and the $(c_n^1, s_n^1, c_n^2, s_n^2)$ are linear combinations of CFFs and nucleon Electromagnetic Form Factors (EFFs). The BH$_i$ amplitudes can be exactly calculated following the expressions

$$|\mathcal{T}_{BH_1}|^2 = -\frac{\xi'(1-\xi)^2}{Q^2\Delta^2 y^4 \tilde{y}^4 \xi(\xi^2-\xi'^2)} \left(\frac{\tilde{y}}{P_1P_2}\right)^2 \sum_{n=0}^{4} \left[c_n^{11}(\varphi_\mu)\cos(n\phi) + s_n^{11}(\varphi_\mu)\sin(n\phi)\right], \tag{18}$$

$$|\mathcal{T}_{BH_2}|^2 = -\frac{\xi'(1-\xi)^2}{Q^2\Delta^2 y^4 \tilde{y}^4 \xi(\xi^2-\xi'^2)} \left(\frac{y}{P_3P_4}\right)^2 \sum_{n=0}^{4} \left[c_n^{22}(\phi)\cos(n\varphi_\mu) + s_n^{22}(\phi)\sin(n\varphi_\mu)\right], \tag{19}$$

$$\mathcal{T}_{BH_{12}} = -\frac{\xi'(1-\xi)^2}{Q^2\Delta^2 y^4 \tilde{y}^4 \xi(\xi^2-\xi'^2)} \frac{y\tilde{y}}{P_1P_2P_3P_4} \sum_{n=0}^{3} \left[c_n^{12}(\varphi_\mu)\cos(n\phi) + s_n^{12}(\varphi_\mu)\sin(n\phi)\right]. \tag{20}$$

The Fourier coefficients write

$$c_n^i(\alpha) = \sum_{m=0}^{2} \left[cc_{nm}^i \cos(m\alpha) + cs_{nm}^i \sin(m\alpha)\right] \tag{21}$$

$$s_n^i(\alpha) = \sum_{m=0}^{2} \left[sc_{nm}^i \cos(m\alpha) + ss_{nm}^i \sin(m\alpha)\right] \tag{22}$$

for $i \equiv (VCS, 1, 2, 11, 12, 22)$ and $\alpha \equiv (\varphi_\mu, \phi)$, correspondingly. The exact expression of each Fourier coefficient is detailed in Ref. [21]. It is worth noticing here that the BH$_i$ propagators exhibit the symmetry properties

$$P_i(\phi) = P_i(2\pi - \phi) \tag{23}$$

$$P_j(\theta_\mu, \varphi_\mu) = P_j(\pi - \theta_\mu, \varphi_\mu + \pi) \tag{24}$$

for $i = \{1, 2, 3, 4\}$ and $j = \{3, 4\}$. As a consequence, the integration over $d\theta_\mu$ in a symmetric interval around θ_μ=$\pi/2$ for any definite moment in θ_μ reduces to a characteristic $\cos(n\varphi_\mu)$ Fourier expansion. Integrating over the muon-pair angles within a θ_0-symmetric interval and quoting only the angular dependencies

$$d^5\sigma^\lambda(\phi) \equiv \frac{d^5\sigma^\lambda(\phi)}{dx_B\, dy\, dt\, dQ'^2\, d\phi} = \int_0^{2\pi} d\varphi_\mu \int_{\pi/2+\theta_0}^{\pi/2-\theta_0} d\theta_\mu \sin(\theta_\mu) \frac{d^7\sigma^\lambda(\phi, \theta_\mu, \phi_\mu)}{dx_B\, dy\, dt\, d\phi\, dQ'^2\, d\Omega_\mu} \tag{25}$$

a DVCS-like 5-fold differential cross section can be obtained as

$$d^5\sigma^\lambda = d^5\sigma_{BH_1} + d^5\sigma_{BH_2} + d^5\sigma_{DDVCS} + d^5\sigma_{\mathcal{I}_1} + \lambda\, d^5\widetilde{\sigma}_{\mathcal{I}_1} = d^5\sigma_{UU} + \lambda\, d^5\sigma_{LU} \tag{26}$$

where, following the symmetries properties of the BH$_2$ amplitude, the BH$_2$ interference contributions vanish; the first index denotes the polarization of the beam $(U, L) \equiv$ (unpolarized, longitudinally polarized), and similarly for the target with the second index. Alternatively, integrating over the azimuthal angle of the final virtual photon

$$d^5\Sigma^\lambda(\varphi_\mu) \equiv \frac{d^5\sigma^\lambda(\varphi_\mu)}{dx_B\, dy\, dt\, dQ'^2\, d\varphi_\mu} = \int_0^{2\pi} d\phi \int_{\pi/2+\theta_0}^{\pi/2-\theta_0} d\theta_\mu \sin(\theta_\mu) \frac{d^7\sigma^\lambda(\phi, \theta_\mu, \phi_\mu)}{dx_B\, dy\, dt\, d\phi\, dQ'^2\, d\Omega_\mu} \tag{27}$$

provides a TCS-like 5-fold differential cross section which can be expressed as

$$d^5\Sigma^\lambda = d^5\Sigma_{BH_1} + d^5\Sigma_{BH_2} + d^5\Sigma_{BH_{12}} + d^5\Sigma_{DDVCS} + d^5\Sigma_{\mathcal{I}_1} + d^5\Sigma_{\mathcal{I}_2} + \lambda\, d^5\widetilde{\Sigma}_{\mathcal{I}_2} = d^5\Sigma_{UU} + \lambda\, d^5\Sigma_{LU}\,. \tag{28}$$

Consequently, experimental observables defined with $d^5\sigma^\lambda$ are sensitive to the interference with the BH$_1$ process which has a relatively large amplitude in the $Q'^2 < Q^2$ region, whereas observables defined with $d^5\Sigma^\lambda$ are sensitive to the interference with the BH$_2$ process of more interest in the $Q'^2 > Q^2$ region. The contribution of the pure BH$_2$ amplitude to the cross section can be further reduced by an appropriate choice of θ_0, $\pi/4$ following the prescription of Ref. [21]. The corresponding cross section, calculated within the VGG framework using the GK19 modeling of GPDs [43, 44], are shown on Fig. 4 for two typical kinematics within the acceptance of the SoLID$_\mu$ spectrometer. Both the DVCS- and TCS-like angular dependences are dominated by the modulations of the BH$_i$ amplitudes with a more prominent number of $\cos(n\varphi_\mu)$ contributions. However, the TCS-like cross section tends to be smaller than the DVCS-like.

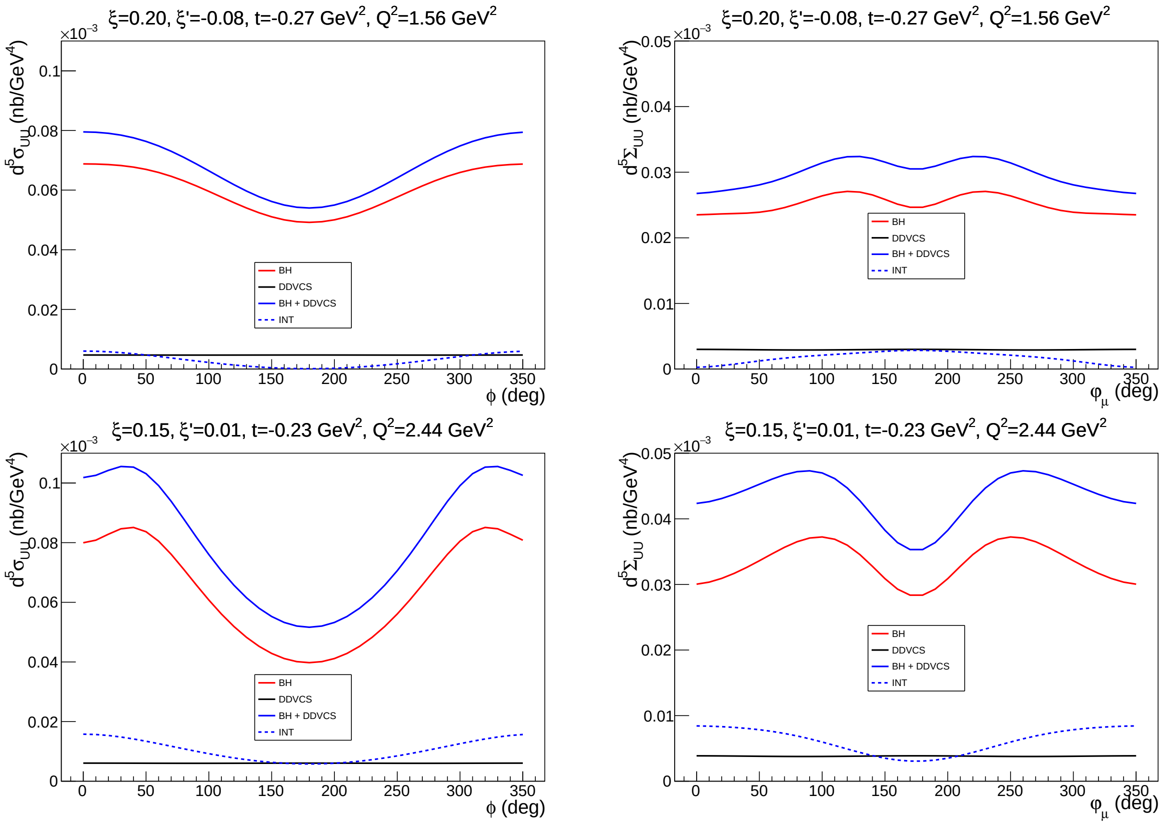

Figure 4: DVCS-(left) and TCS-like(right) differential cross sections for typical kinematics within the acceptance of the SoLID$_\mu$ spectrometer.

2.2.2 Beam spin asymmetry

The interference amplitudes between the BH and DDVCS processes are observables of interest because of their linear relationship with CFFs. From Eq. (26) and Eq. (28), it is readily seen that the beam helicity dependence of the cross section allows us to isolate the helicity dependent part of the $\mathcal{I}_i^\lambda$ amplitudes. The Beam Spin Asymmetry (BSA) observables can be defined as

$$A_{LU}^{\sigma^\lambda} \equiv A_{LU}^{\sigma^\lambda}(\phi) = \lambda \, \frac{d^5\sigma^+ - d^5\sigma^-}{d^5\sigma^+ + d^5\sigma^-} = \frac{\lambda \, d^5\widetilde{\sigma}_{\mathcal{I}_1}}{d^5\sigma_{BH_1} + d^5\sigma_{BH_2} + d^5\sigma_{DDVCS} + d^5\sigma_{\mathcal{I}_1}} \tag{29}$$

$$A_{LU}^{\Sigma^\lambda} \equiv A_{LU}^{\Sigma^\lambda}(\varphi_\mu) = \lambda \, \frac{d^5\Sigma^+ - d^5\Sigma^-}{d^5\Sigma^+ + d^5\Sigma^-} = \frac{\lambda \, d^5\widetilde{\Sigma}_{\mathcal{I}_2}}{d^5\Sigma_{BH_1} + d^5\Sigma_{BH_2} + d^5\Sigma_{BH_{12}} + d^5\Sigma_{DDVCS} + d^5\Sigma_{\mathcal{I}_1} + d^5\Sigma_{\mathcal{I}_2}} \tag{30}$$

where only the azimuthal angular dependence of the observables was quoted. The LU indexes denote a longitudinally polarized beam and an unpolarized target. Similarly to DVCS and TCS, these observables access the imaginary part of a linear combination of CFFs. Most notably, $d^5\widetilde{\sigma}_{\mathcal{I}_1}$ and $^5\widetilde{\Sigma}_{\mathcal{I}_2}$ access the same GPD content of the nucleon *i.e.*

$$A_{LU}^{S^\lambda} \propto \Im\mathrm{m}\left\{ F_1 \mathcal{H} + \xi'(F_1 + F_2)\widetilde{\mathcal{H}} - \frac{t}{4M_N^2} F_2 \mathcal{E} \right\} , \tag{31}$$

a feature of particular interest for experimental consistency. BSA observables are shown on Fig. 5 for two kinematics within the SoLID$_\mu$ acceptance. Calculations have been obtained from the VGG modeling of observables using either VGG or GK19 GPDs. As expected, BSAs are changing sign with the sign of ξ' and are somehow sensitive to the GPD model. Because of smaller unpolarized cross sections, TCS-like BSAs have larger amplitude than DVCS-like ones.

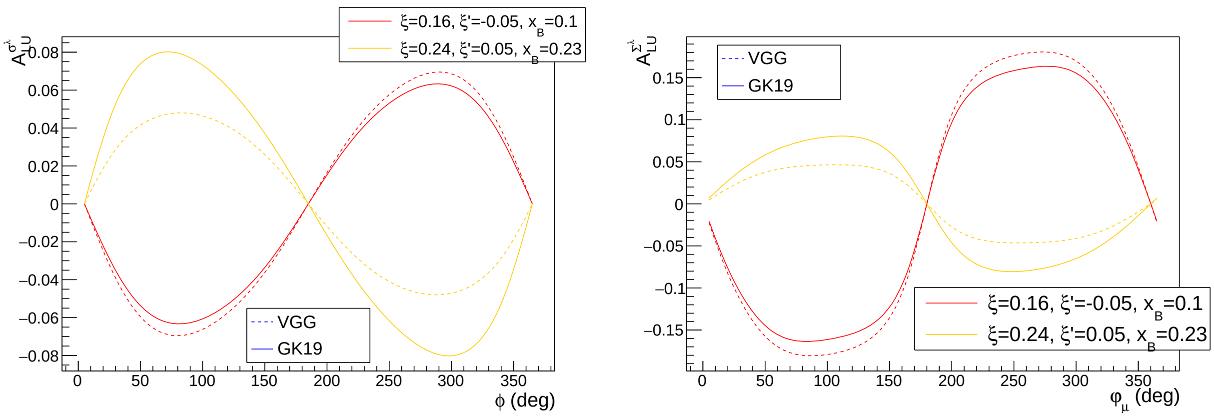

Figure 5: DVCS-like (left) and TCS-like (right) BSAs for typical kinematics within the acceptance of the SoLIDμ spectrometer and different GPD models.

2.2.3 Muon charge asymmetry

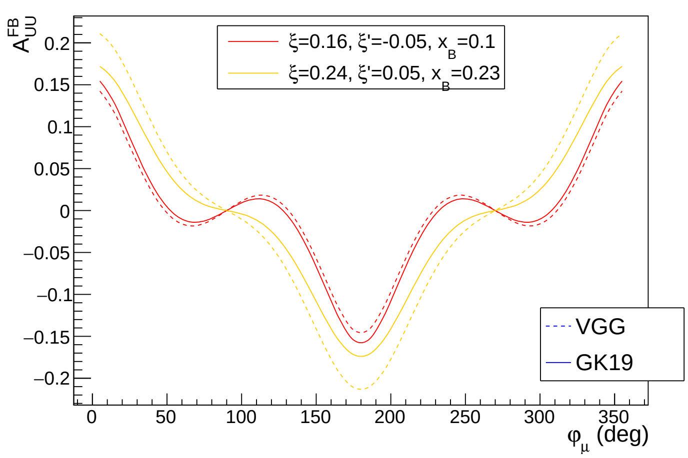

Figure 6: μCAs for the same kinematics as Fig. 5 and computed following the same prescriptions.

As in the case of TCS, charge conjugation asymmetries can be accessed with DDVCS without changing the electric charge of the beam. Indeed, the Forward-Backward (FB) asymmetry in the $\mu^+\mu^-$-pair production cross-section, which has been a key observable of the first measurement of TCS at JLab [18], can similarly be accessed with DDVCS thus enabling the investigation of the real part of DDVCS CFFs in a leading twist and leading α_S-order approach. This is even more of interest than there is to-date no dispersion relationship between the real and imaginary parts of the DDVCS CFFs, contrary to DVCS/TCS. The DDVCS FB asymmetry or muon charge asymmetry can be defined as

$$A_{UU}^{FB}(\varphi_\mu) = \frac{d^5\Sigma_{UU}(\varphi_{\mu^-}) - d^5\Sigma_{UU}(\varphi_{\mu^-}+\pi)}{d^5\Sigma_{UU}(\varphi_{\mu^-}) + d^5\Sigma_{UU}(\varphi_{\mu^-}+\pi)} = \frac{d^5\Sigma_{UU}(\varphi_{\mu^-}) - d^5\Sigma_{UU}(\varphi_{\mu^+})}{d^5\Sigma_{UU}(\varphi_{\mu^-}) + d^5\Sigma_{UU}(\varphi_{\mu^+})} = A_{UU}^{\mu^\pm}(\varphi_\mu) \tag{32}$$

with

$$d^5\Sigma_{UU}(\varphi_{\mu^-}+\pi) = \int_0^{2\pi} d\phi \int_{\pi/2+\theta_0}^{\pi/2-\theta_0} d\theta_{\mu^-} \sin(\theta_{\mu^-}) \frac{d^7\sigma^0(\phi, \pi-\theta_{\mu^-}, \varphi_{\mu^-}+\pi)}{dx_B\, dy\, dt\, d\phi\, dQ'^2\, d\Omega_{\mu^-}} \tag{33}$$

$$= \int_0^{2\pi} d\phi \int_{\pi/2+\theta_0}^{\pi/2-\theta_0} d\theta_{\mu^+} \sin(\theta_{\mu^+}) \frac{d^7\sigma^0(\phi, \theta_{\mu^+}, \varphi_{\mu^+})}{dx_B\, dy\, dt\, d\phi\, dQ'^2\, d\Omega_{\mu^+}} = d^5\Sigma_{UU}(\varphi_{\mu^+})\,. \tag{34}$$

Following angular properties of the reaction amplitudes, the previous equality can be recast as

$$A^{\mu^\pm}_{UU}(\varphi_\mu) = \frac{d^5\Sigma_{BH_{12}} + d^5\Sigma_{\mathcal{I}_2}}{d^5\Sigma_{BH_1} + d^5\Sigma_{BH_2} + d^5\Sigma_{DDVCS} + d^5\Sigma_{\mathcal{I}_1}} \tag{35}$$

which indicates that the Muon Charge Asymmetry (μCA) is generated from the interference of the BH$_2$ process with the other contributions (BH$_1$ and DDVCS) to the di-muon pair production cross section. Although the μCA receives some contribution of the interference between the BH$_i$ process, this precisely calculable part turns out to be non-dominant and thus can be straightforwardly subtracted. Finally, muon charge asymmetries access the GPD content of the nucleon through

$$d^5\Sigma_{\mathcal{I}_2} \propto -\frac{\xi'}{\xi}\Re\mathfrak{e}\left[F_1\mathcal{H} + \frac{\xi^2}{\xi'}(F_1+F_2)\widetilde{\mathcal{H}} - \frac{t}{4M_N^2}F_2\mathcal{E}\right]. \tag{36}$$

It is worth noting that, differently from DVCS and TCS, BSAs and μCAs are sensitive to different CFF combinations. Particularly, the contribution of $\mathcal{H}$ to the real part can be suppressed by an appropriate choice of kinematics enabling more sensitivity to $\widetilde{\mathcal{H}}$ than for the imaginary part. The same GPD content can be obtained from the FB asymmetry of $d^5\sigma$, however with a more intricate contribution of the pure BH$_i$ amplitudes. $A^{\mu^\pm}_{UU}$ is shown on Fig. 6 for typical kinematics within the SoLID$_\mu$ acceptance and computed with the VGG description of experimental observables using the VGG and GK19 modeling of GPDs, similarly to previous evaluations of BSAs (see Sec. 2.2.2). The rich φ_μ-modulation and the large variation of the expected signal are making a very promising observable.

3 Impact of DDVCS measurements

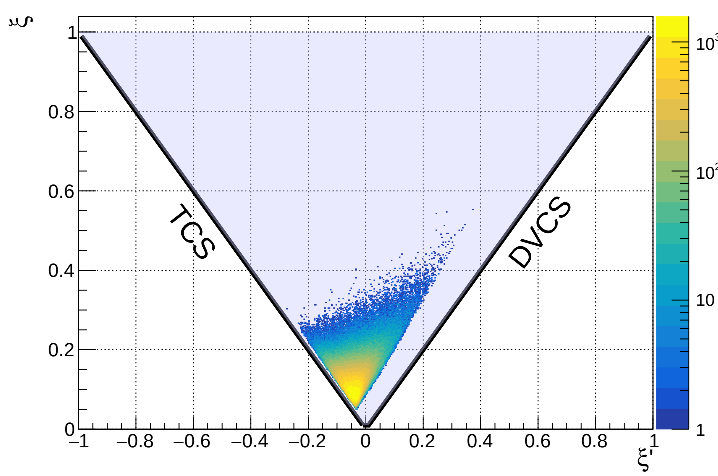

Figure 7: (ξ', ξ) phase space of the DDVCS reaction where the ξ=ξ' and ξ=-ξ' trajectories correspond to the DVCS and TCS limits, respectively; the superposed multi-coloured area indicates the phase-space coverage of the here-proposed SoLID$_\mu$ experiment.

The essential benefit of the DDVCS reaction is to provide the experimental possibility to explore the (ξ', ξ) phase space supporting GPDs at $\xi \neq \pm\xi'$ (Fig. 7), that is for instance to access the skewness dependency of GPDs at a fixed generalized Bjorken variable. This translates into the measurement of GPDs at $\xi \neq \pm\xi'$ via the imaginary part of CFFs and the sampling of GPDs at $\xi \neq \pm\xi'$ via the real part of CFFs (Eq. (3)). These basic facts have direct consequences on the knowledge of several key-features of the nucleon structure.

3.1 Nucleon tomography

GPDs provide new visual insight on the partonic structure of matter by allowing for a tomography of the nucleon [9, 11]. In the particular case of zero skewness, GPDs acquire a well-defined probability interpretation in the infinite momentum frame, similarly to conventional parton distributions. For instance, the impact parameter dependent parton distribution related to H^q can be written [45]

$$q(x, \mathbf{b}_\perp) = \frac{1}{(2\pi)^2} \int d^2\mathbf{\Delta}_\perp \, H^q(x, 0, -\mathbf{\Delta}_\perp^2) \, e^{-i\mathbf{b}_\perp \cdot \mathbf{\Delta}_\perp} \tag{37}$$

telling that $q(x, \mathbf{b}_\perp)$ is the Fourier transform of $H^q(x, 0, -\mathbf{\Delta}_\perp^2)$. Consequently, the knowledge of GPDs at zero skewness allows to determine the probability to find a parton carrying the light-cone longitudinal momentum fraction x of the nucleon at a transverse distance $\mathbf{b}_\perp$ from the center of momentum. In that respect, recent lattice calculations at the physical pion mass predict that the parton density probabililty rapidly decrease as x increases (Fig. 8).

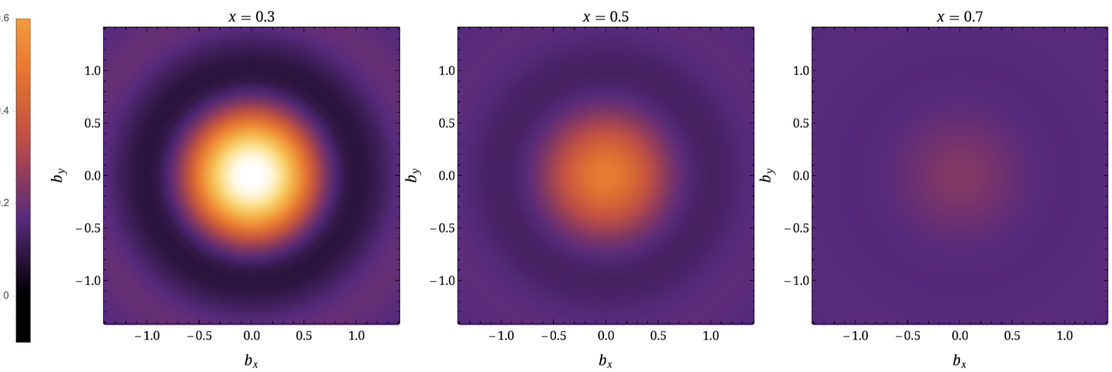

Figure 8: 2-dimensional representation of the momentum dependent impact parameter parton distribution function of the GPD H, from lattice calculations at physical pion mass at different x [46].

On the experimental side, existing data provide only a limited support for such a representation. The access to 0-skewness GPDs for any momentum fraction x is obtained from a strongly under-constrained and model dependent interpretation of DVCS data allowing to extrapolate the ξ-dependence of H [47]. Bringing new GPDs information at $\xi \neq \pm x$ will constrain the theoretical knowledge of the skewness dependence of GPDs. Ultimately, DDVCS will enable a model-independent determination of the ξ-dependence, providing a truly experimental determination of the parton transverse densities.

3.2 Gravitational form factors

Similarly to the encoding of the electromagnetic structure of the nucleon through the matrix element of the electromagnetic current, the matrix elements of the Energy-Momentum Tensor (EMT) of the nucleon contain information about the mass, spin and mechanical properties of the nucleon [48]. These are encoded in terms of the so-called EMT Gravitational Form Factors (GFFs) which may be written for quarks and gluons ($a \equiv q, g$) as[3]

$$\begin{aligned}\langle p', \vec{s}' | T^a_{\mu\nu} | p, \vec{s} \rangle = \bar{u}(p', \vec{s}') \Bigg\{ & \frac{P_\mu P_\nu}{M} M_2^a(t) + \frac{\Delta_\mu \Delta_\nu - g_{\mu\nu}\Delta^2}{M} C^a(t) + M g_{\mu\nu} \bar{C}^a(t) \\ & + \frac{P_{\{\mu} i\sigma_{\nu\}\rho}\Delta^\rho}{2M} J^a(t) + \frac{P_{[\mu} i\sigma_{\nu]\rho}\Delta^\rho}{4M} D^a(t) \Bigg\} u(p, \vec{s})\end{aligned} \tag{38}$$

[3]The notation $v_{\{\mu}w_{\nu\}} = v_\mu w_\nu + v^\nu w_\mu$ and $v_{[\mu}w_{\nu]} = v_\mu w_\nu - v_\nu w_\mu$ is used.

with $P=(p+p')/2$ and where $M_2^a(t)$ represents the mass/energy distribution inside the nucleon, $J^a(t)$ the total angular momentum distribution, and $C^a(t), \bar{C}^a(t)$ the forces distribution. For instance, the Fourier transform of $C(t) \equiv \sum_a C^a(t)$ allows us to infer the mechanical radius of the nucleon and the distribution of pressure and shear forces inside the nucleon [49]. GFFs may be probed indirectly in various exclusive processes including DVCS, TCS, J/Ψ production at threshold, and DDVCS. Particularly, the D-term parameterizing the GPDs is accessed via DVCS through the dispersion relationship between the real and imaginary parts of the $\mathcal{H}$ CFF which writes at leading order

$$\mathfrak{Re}\left[\mathcal{H}(\xi,t)\right] = \mathcal{C}_{\mathcal{H}}(t) + \mathcal{P}\left\{\int_{-1}^{1}\left[\frac{1}{\xi-x} - \frac{1}{\xi+x}\right]\mathfrak{Im}\left[\mathcal{H}(x,t)\right]\,dx\right\} \tag{39}$$

where the subtraction constant at leading twist and leading order in α_s can be written as

$$\mathcal{C}_{\mathcal{H}}(t) = 2\sum_q e_q^2 \int_{-1}^{1} \frac{D^q_{\mathrm{term}}(z,t)}{1-z}\,dz = 2\sum_q e_q^2 \int_{-1}^{1} (1+z) \sum_{2n+1} d_n^q(t)\, C_n^{3/2}(z)\,dz \tag{40}$$

with

$$C^q(t) = \frac{1}{5} d_1^q(t)\,. \tag{41}$$

Thus, the separate measurements of the real and imaginary part of $\mathcal{H}$ provide a measurement of the subtraction constant which in turn leads to the so-called Polyakov-Weiss D-term which relates to the $C^q(t)$ GFF. While $\mathfrak{Im}[\mathcal{H}]$ is obtained directly from the helicity dependent part of the DVCS cross section, beam of different charges are required to isolate $\mathfrak{Re}[\mathcal{H}]$ from the DVCS cross section [50]. It is indeed a key-measurement of the Positron Physics Program [51] at the future Ce$^+$BAF [52]. On the basis of existing data, $C^q(t)$ can be obtained from the previous multi-step procedure only using the guidance of theoretical GPD ansatzs [53].

DDVCS provides another alternative to access the D-term taking advantage of the polynomiality properties of GPDs. This major property expresses that the $(n+1)^{\mathrm{th}}$ Mellin moment of a GPD is a polynomial in ξ of maximal $n+1$ order, that is considering H

$$\int_{-1}^{1} dx\, x^n \sum_q H^q(x,\xi,t) = \sum_{i=0}^{n+1} \sum_q h_i^{q(n)}(t)\, \xi^n\,. \tag{42}$$

For instance, the second Mellin moment of the GPD H can be expressed as [6]

$$\int_{-1}^{1} dx\, x \sum_q H^q(x,\xi,t) = \sum_q M_2^q(t) + \frac{4}{5}\sum_q d_1^q(t)\,\xi^2 \tag{43}$$

which relates the 2nd Mellin moment with GFFs, particularly its skewness dependence with the D-term. Measuring GPDs at $\xi' \neq \pm\xi$, DDVCS provides experimental information to constrain the calculation of the left-hand side integral at fixed skewness. The imaginary part of CFFs is a direct constrain on the theoretical modelling of GPDs, while the real part of CFFs helps to constrain the region $|\xi'| < \xi$ lying outside the physics phase space accessible to Compton-like exclusive reactions.

3.3 Deconvolution of Compton form factors

The determination of GPDs from experimental observables is a difficult problem which starts with the reaction selected to probe the partonic structure of the nucleon. For instance, Compton-like processes directly access GPDs while deeeply virtual meson production combines the partonic information of both the nucleon and the produced meson. Nevertheless, Compton-like processes do not generally access a single CFF but a linear and/or bi-linear combination of CFFs which depends on the target polarization. Thus, several different experimental observables with different sensitivity to a specific CFF are required to determine from experimental data the 8 unknown quantities corresponding to the real and imaginary parts of the nucleon helicity conserving CFFs $(\mathcal{H}, \mathcal{E}, \widetilde{\mathcal{H}}, \widetilde{\mathcal{E}})$. The situation becomes even more complex when considering higher-twist effects and higher α_S-orders.

Several methods based on the fitting of experimental data have been developed to extract CFFs. In local fit approaches [54, 55, 56], all experimental observables at a fixed kinematical point of the physics phase-space are considered to obtain a model independent extraction of CFFs. This last feature is both an advantage and a drawback of this technique which does not take into account the physics properties of CFFs and commonly leads to large error bars due to the limited number of observables and the induced correlation between the deduced CFFs.
In global fit approaches [57, 58, 59], a simultaneous fit of the world data set is performed within the guidance of theoretical models ensuring basic physics properties and limits of GPDs. Such a global fit is statistically more precise than a local fit but potentially less selective with respect to the different theoretical prescriptions which parameters are fitted against experimental data. Novel techniques based on Artificial Neural Networks [60, 61, 62] have been proposed. These advanced techniques are most promising since they preserve the physics constraints while allowing for a model independent global fit.

Extracting GPDs from CFFs, known as the deconvolution problem, is the last step of the process providing an experimental determination of GPDs. Because of the integral nature of CFFs, it implies the knowledge of GPDs in the full (ξ', ξ, t) physics phase space, which cannot be achieved with DVCS and TCS only. Furthermore, it was shown that the deconvolution problem does not accept a unique solution but a class of functions fulfilling the required physics constraints and resulting in different GPDs for the same observables [63]. The only way to remove this degeneracy is to bring information from other channels. Exploring the physics phase space away from the diagonal $\xi'=\pm\xi$, the DDVCS reaction will provide additional constraint on this problem and will help the convergence of the GPD-deconvolution from DVCS and TCS CFFs towards a unique solution.

4 Experimental setup

4.1 SoLIDμ spectrometer

The experiment E12-12-006 [64] was approved to measure J/ψ near threshold of J/ψ at 11 GeV. And the E12-12-006A [65] Timelike Compton Scattering (TCS) experiment for GPD study was also approved as a run group experiment using the same setup. We are proposing to supplement the J/ψ setup with a new forward angle muon detector (FAMD) for the DDVCS measurement. It will form the new SoLIDμ setup as shown in Fig. 9. The data taking can happen for the three experiments at the same time with a proper trigger configuration as described in the following sections.

SoLID will be an all-new spectrometer in Hall A during the 12 GeV era [66]. It is designed to use a solenoid magnet to sweep away low-energy charged background particles, and can thus carry out experiments using high-energy electron beams incident on unpolarized or polarized targets at luminosities up to $L = 1.2 \times 10^{37}$ cm^{-2} sec^{-1} in the J/ψ setup. It has two groups of detectors. The forward-angle detectors cover polar angle from 8.5° to 16.5° and consist of several planes of Gas Electron Multipliers (GEM) for tracking, a light-gas Cherenkov (LGCC) for e/π separation, a heavy gas Cherenkov (HGCC) for π/K separation, a Multi-gap Resistive Plate Chamber (MRPC) for time-of-flight, and an Electromagnetic Calorimeter (FAEC). The large-angle detectors cover polar angle from 18° to 30° and consist of several planes of GEM for tracking, and an Electromagnetic Calorimeter (LAEC). Particles in SoLID will be detected and identified by measuring their momenta, time-of-flight, number of photons produced in the threshold Cherenkov detectors, and energy losses in the calorimeters and MRPC.

The SoLID solenoid will reuse the CLEO-II magnet. Its superconducting coil and cryostat remains unchanged. It has a large inner space with a clear bore diameter of 2.9 m and a coil of 3.1 m diameter. The coil length is 3.5 m, with a 3.8 m long cryostat. The coil is made of 5×16 mm^2 aluminum-stabilized superconductor, and runs at 3300 A. Part of the CLEO-II iron flux return will be modified and reused, and two new iron endcaps will be added at the front and back of the solenoid. The axial central field of the solenoidal magnet can reach about 1.4 T.

Six layers of GEM detectors will be used for tracking, providing information on the momentum, angle, and interaction vertex of the detected particles. They will be placed uniformly inside the solenoid magnet.

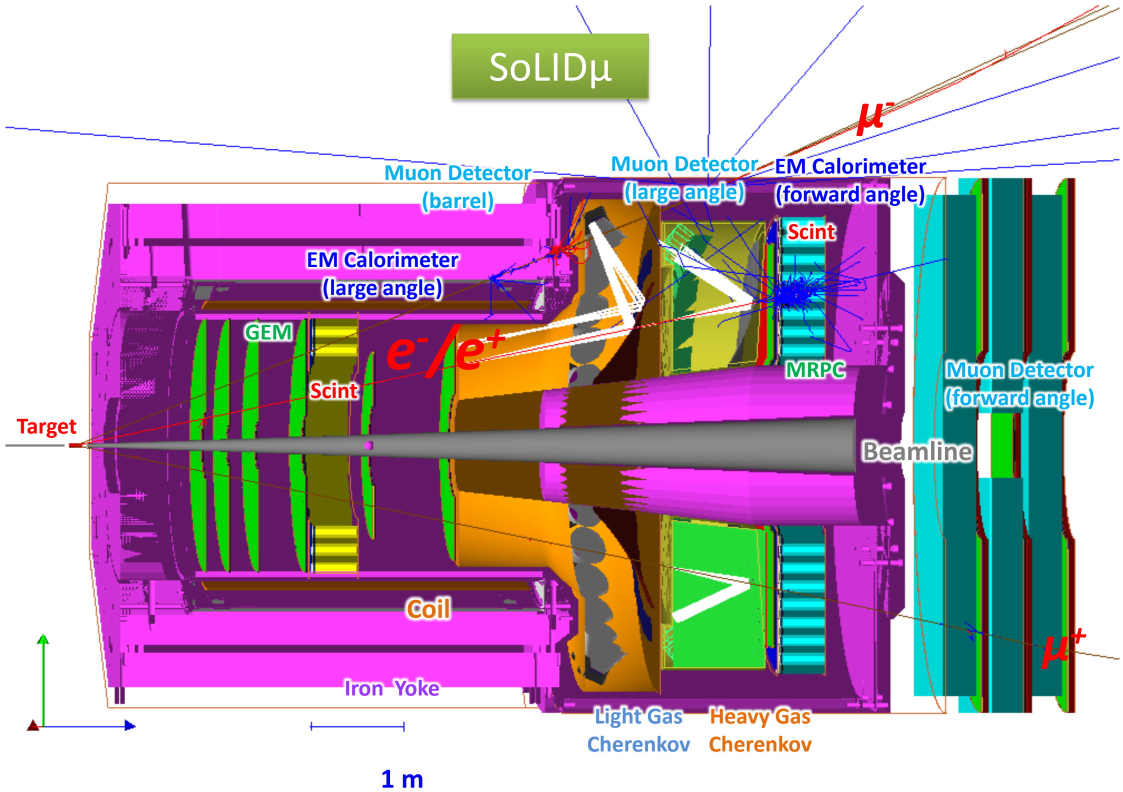

Figure 9: SoLIDμ as SoLID J/ψ setup with the forward angle muon detector added, shown in its Geant4 simulation.

For the forward angle detectors, five layers except for the first layer of GEM detectors will be used. In principle, three points are needed to reconstruct the kinematic variables. The fourth and fifth points will bring enough redundancy to compensate for the inefficiency of the GEM tracking detector. For the large-angle detectors, four layers of GEMs detector except the last two layers will be used. In this case, four layers are enough since the background level at large angles is expected to be smaller. SoLID GEMs will provide full azimuthal angular coverage by using trapezoidal-shaped sectors. The area of a single sector can be as large as 100 cm $\times$ 40 cm. Recent advancements in technology, like single-mask GEM etching and GEM splicing, makes it possible to fabricate GEM foils up to 100 cm $\times$ 200 cm. The GEM readout is by 2D strips readout by VMM chips developed for ATLAS Small Wheel Micromegas detectors.

The Cherenkov detectors at forward angles have two parts. The light-gas one uses a standard CO_2 gas radiator and can provide e/π separation up to momenta of 4.9 GeV/c with pion rejection in order of 10^3. The heavy-gas one uses C_4F_8 gas at 1.7 atm and gives a momentum threshold of 2.5 GeV/c and 7.5 GeV/c for pions and kaons, respectively. In both cases, the Cherenkov light is directed by the mirror systems onto Multi-Anode PMTs (MAPMTs) for readout.

There is one electromagnetic calorimeter at forward angles and one at large angles. They are made with identical Shashlyk-type modules. Each module is made of a pre-shower and a shower part. The pre-shower detector is simply a 2 radiation-length lead layer and a 2 cm thick scintillator with embedded wave-length-shifting (WLS) fibers for readout. The shower detector is of Shashlyk type, consisting of about 200 layers of 0.5 mm lead and 1.5 mm scintillator, and many WLS fibers penetrating all layers with a density about 1/cm^2 for readout at the back of a module. This type of design can reach a pion rejection factor of more than 100, with good electron efficiency. Its radiation hardness is in the order of 500 krad, which satisfies the high-luminosity condition in SoLID.

MRPC-based time-of-flight systems have recently been used in the RHIC STAR and LHC ALICE experiments, providing a typical time resolution close to 100 ps. With readout strips, it can work inside a magnetic field. Using low-resistive glass, it can gain even an higher rate capability. SoLID experiments have a forward-angle MRPC as part of the planned baseline equipment.

Scintillator pad detector (SPD) will placed at both forward and large angle. FASPD will provide combined photon rejection with MRPC, but TOF will rely on MRPC for its better time resolution of 100 ps. LASPD will provide both photon rejection and TOF with time resolution of 150 ps.

4.2 Muon detector

For the forward angle muon detector, we will reuse the iron plates from the CLEO II magnet. Only two inner layers are planned to be used for the barrel part of the SoLID magnet. The third and most outer layer of iron made of 8 iron plates about 533x250x36 cm long are left used. 7 of the 8 plates are currently stored at JLab and we will reuse the 6 of the 7 plates for the forward angle muon detector. We are planning to lay the iron in 3 layers and following each plate of iron with a tracking detector and a scintialtor detector, as show in Figure 10. There is no known conflict in term of space and engineering concern for the planned muon detector location. A preliminary concept design of the iron plate holder by an engineer from the Orsay group is shown in Figure 11. A TOSCA field calculation confirmed the solenoid field has almost no effect on those iron plates with the forces at the order of one Newton and the torques at the order of 2 N-m.

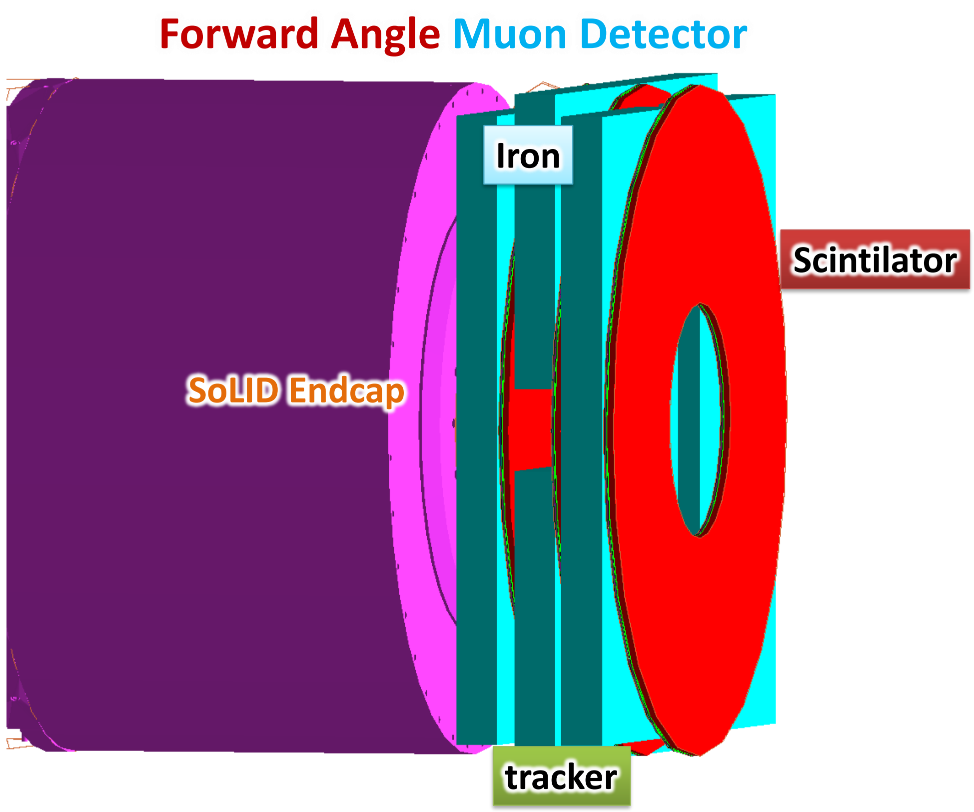

Figure 10: Preliminary design of SoLID muon detector at forward angle in Geant4 simulation.

The 3 layers of tracking detectors and scintillator detectors can be mounted on their own frame independent of the iron layers. Each layer needs to cover roughly a full donut shape with an inner radius of

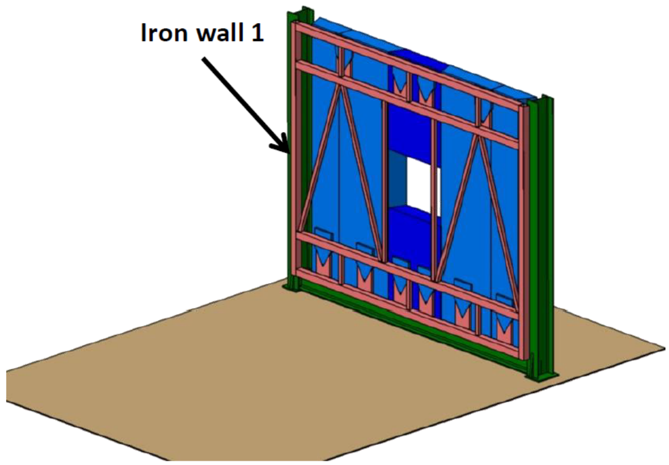

Figure 11: Preliminary design by Orsay engineer of holder for the iron plates

1 m and a outer radius of 3 m, which is about 25 m^2 in area. The total area is about 75 m^2. The 3 trackers will reconstruct straight muon or background pion tracks and connect that with the track detected by the existing SoLID inner GEM trackers. Because of the 10 m long flight path and heavy materials along the way, the multiple scattering can make the two segments of tracks can reach 10 cm. But it is not a problem because the particle rate at the muon detector are low as shown in the simulation sections. The 3 scintillator planes will measure the energy deposition of muon or background pion, while the latter often has hadronic showers and deposit more energies with larger spread than the former. Multiple layers with proper segmentations can help separate pion showers from the minimum ionizing muon. The 3rd or last plane of scintillator will also serve as part of trigger system because it has the best muon/pion ratio after pion blocking by all the materials. The detector design is ongoing with simulation studies, We will describe some of possible hardware options as follows.

Micropattern Gaseous Detector (MGPD) are widely used as tracking detectors with good resolution and rate capability. Depending on the budget size, currently there are three different options for composing a muon detector tracking system using MGPD.

Option 1 is to use μRWell technology. this technology was introduced in the mid-2010s as a robust, high-rate capable detector with built-in spark protection using a resistive layer. In reality, the amplification layer is etched directly on top of the readout strip layers, forming only one key component layer. The cost can be greatly reduced compared with traditional GEM detectors. This technology is adopted by the EIC outer barrel tracking detector as well (Fig. 12). However, for EIC application, an extra GEM layer was added to make the detector gain larger for a better position resolution. This GEM layer is optional for our muon detector case, as we don't need high position resolution. The total cost for EIC μRWELL PCB is 25K, the size is roughly 1.8 meters by 0.5 meters. To make a full layer of muon tracker detector, this size is roughly in the same scale as the muon tarcker would need, see Figure 13. The average cost reduces if more units are ordered, therefore, it is safe to estimate that for a full muon tracking layer, the cost can be controlled within 300K.

Option 2 is to use new GEM detectors dedicated for the muon trackers. One promising point is that the JLab MPGD center will be completed in a 3 year scale, and the MPGD center will have the capability to produce large GEM foils. Given that most of the cost on the GEM detectors is related to tooling and labor, when the JLab MPGD center completes, the cost for constructing large area GEM detectors for SoLID will be greatly reduced. Here for a comparison, the cost for manufacturing one layer of muon GEM trackers in CERN is roughly 400K.

Option 3 is to reuse the GEM detectors from the current SBS experiments and MOLLER experiments. The current SBS spectrometers have in total of 16 layers, each layer is roughly 2 meters by 0.5 meters, MOLLER experiments have in total of around 40 chambers, each chamber is about 50 cm by 40 cm. All these GEM detectors can cover a total area of 22 m^2, which is roughly one layer, therefore reducing the cost by one layer.

The readout electronics is another major topic for the muon trackers, however, the cost for readout electronics can be greatly reduced by reusing the SBS MPD electronics, where the current SBS program has roughly around 200K channels. The readout channels can also be further reduced by using the charge sharing technology. Depending on the experiment singles rate requirements, the charge sharing technology can reduce the total readout channels by a factor of 2 to 8 while maintaining the same position resolution.

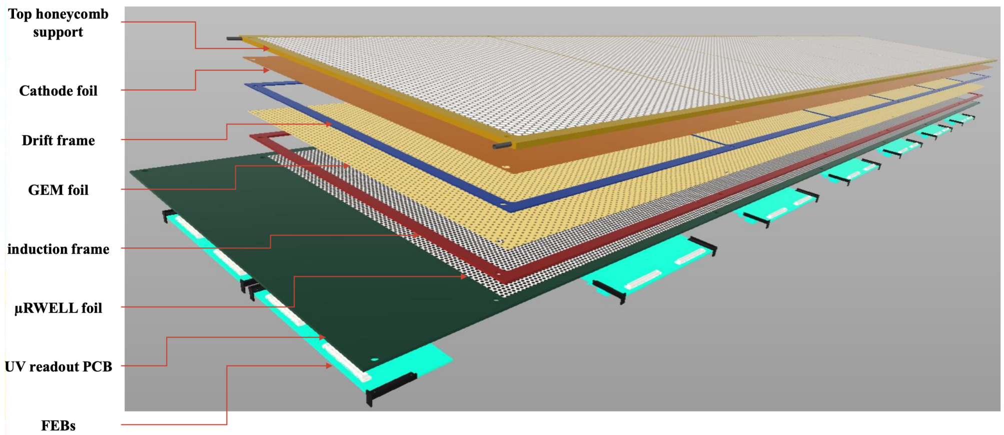

Figure 12: μRWELL Hybrid Tracker Detector for EIC.

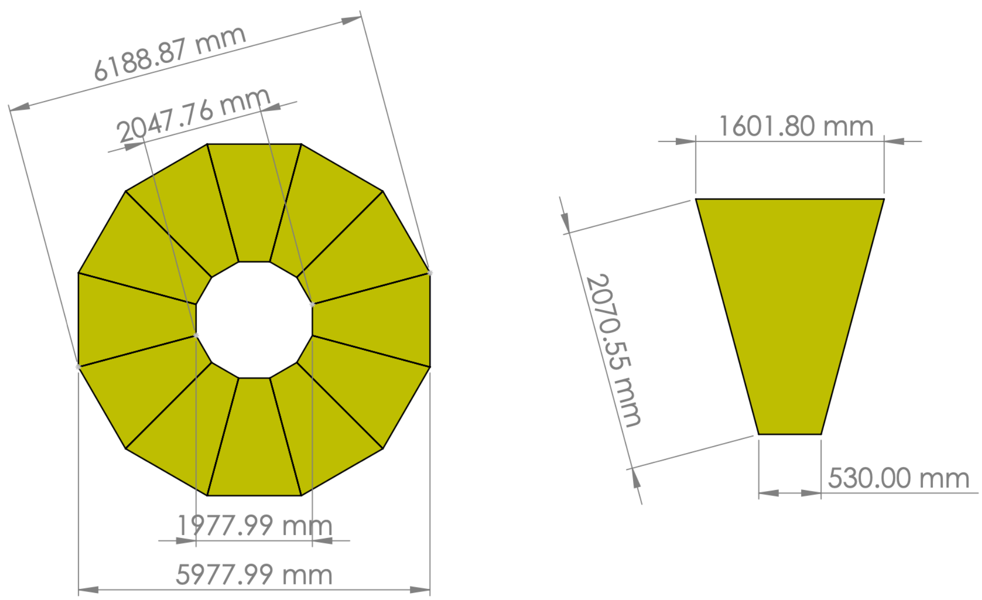

Figure 13: muon Tracking Layer.

Scintillators for the muon detector only needs have good energy measurement for the muon/pion separation and good timing resolution for coincidence with other detectors and triggering purposes. Plastic scintillators with about 5 cm thickness can work well at the relatively low rate environment and reach about 100ps timing resolution. Each plane could have 30 sectors in the azimuthal direction to match the inner segmentation of SoLID inner detectors. To read out the large area Scintillators, wavelegnth shifting fibers can be embedded in them to transport lights to PMTs at the boundaries. many other detectors and SoLID inner scintillators use the same technique.

4.3 Data acquisition

The GEM readout was initially designed to use the APV25 for the readout but is switching to VMM3 readout. The VMM3 chip is a 64 channels ASIC providing time and amplitude for each channel, a prototype for SoLID GEM readout was developed to be able to handle up to 10 MHz per channel.

Most photosensors are readout using JLab FADC 250 MHz which are 16 channels VME board sitting in a VXS crate. The VXS backplane has 4 point to point high speed serial connection up to 5 Gbps, this allows to create a trigger based on FADC data. One unused lane from FADC was used for Fast Readout of FADC, increasing the data rate from about 100 MB/s to 500 MB/s, effectively increasing the bandwidth by a factor 80 since boards can be read out in parallel. This allows to transfer the FADC data at higher rate to reach a trigger rate of 200 KHz, as the baseline maximum rate for the experiment.

Since muons leave low energy in the calorimeter, a dedicated muon triggers has to be developed based on the muon detectors located after the calorimeter. Indeed since muons are heavy leptons they radiate much less than electrons and can get through large amount of materials. The signal for triggering will be provided by muon trigger scintillator plane signals that will be further fed into a JLab custom logic module. It is a 250 MHz pipeline module able to built coincidence every 4 ns at 1 ns resolution. The trigger will search for coincidence between several layers of trackers looking for zone of interest and clean tracks. The muon trigger will look for the coincidence of two candidate muon tracks to reduce the effect of single pion/muon background. The main trigger will be a coincidence between the standard calorimeter trigger and the muon detector. Additional lower level triggers would also be implemented for a precise understanding of the detectors acceptances and efficiencies.

The J/ψ experiment triggers are positron and electron in calorimeter and light gas Cerenkov for photoproduction with about 60 kHz trigger rate. To run DDVCS in parallel, an additional di-muon trigger will be set up. Singles rate in muon detector is mostly dominated by pion and muon from pion decay. Rates were about 300 KHz for each polarity, giving a 600 KHz total single rates. Assuming a 50 ns coincidence window this gives about 20 KHz dimuon trigger rate. Total expected trigger rate is thus about 80 KHz, which is well within the DAQ capabilities of 100 KHz.

more content will be added

5 Simulation studies

We conducted the simulation study using the SoLID Geant4 program "solid_gemc" with the SoLIDμ setup including all subsystems. It helps us understand the acceptance of the signal events and contamination of background. It also provides information about detector response and rate.

5.1 Acceptance

We plan to mainly detect the 3 fold topology of scattered electrons and decay muons to reconstruct the DDVCS reaction. Single particle acceptance for both electron and muon are studied by throwing them evenly into the setup from the target location with vertex covering the full target length of 15 cm. The expected acceptance in polar angle and momentum is shown on Fig. 14. The low momentum cut off for electrons is mostly from magnetic field and SoLID forward angle boundary, while the low momentum cut off for muon near 2 GeV is mainly from materials blocking. Both geometry and decay effect are included in this study. However to count for PID and tracking efficiency, we estimate the total muon efficiency about 87% and total electron efficiency about 90%. The total efficiency for one electron and two muons thus is about 70%. The recoil protons can also be detected by time of flight detector and tracking and their acceptance is similar the scattered electrons. This 4 fold topology will provide the cleanest data samples but with lower statistics. The other 3 fold topology of recoil proton and decay muons can also be detected, but it would be overwhelmed by the real photon BH events and thus hard to be used for the DDVCS physics analysis.

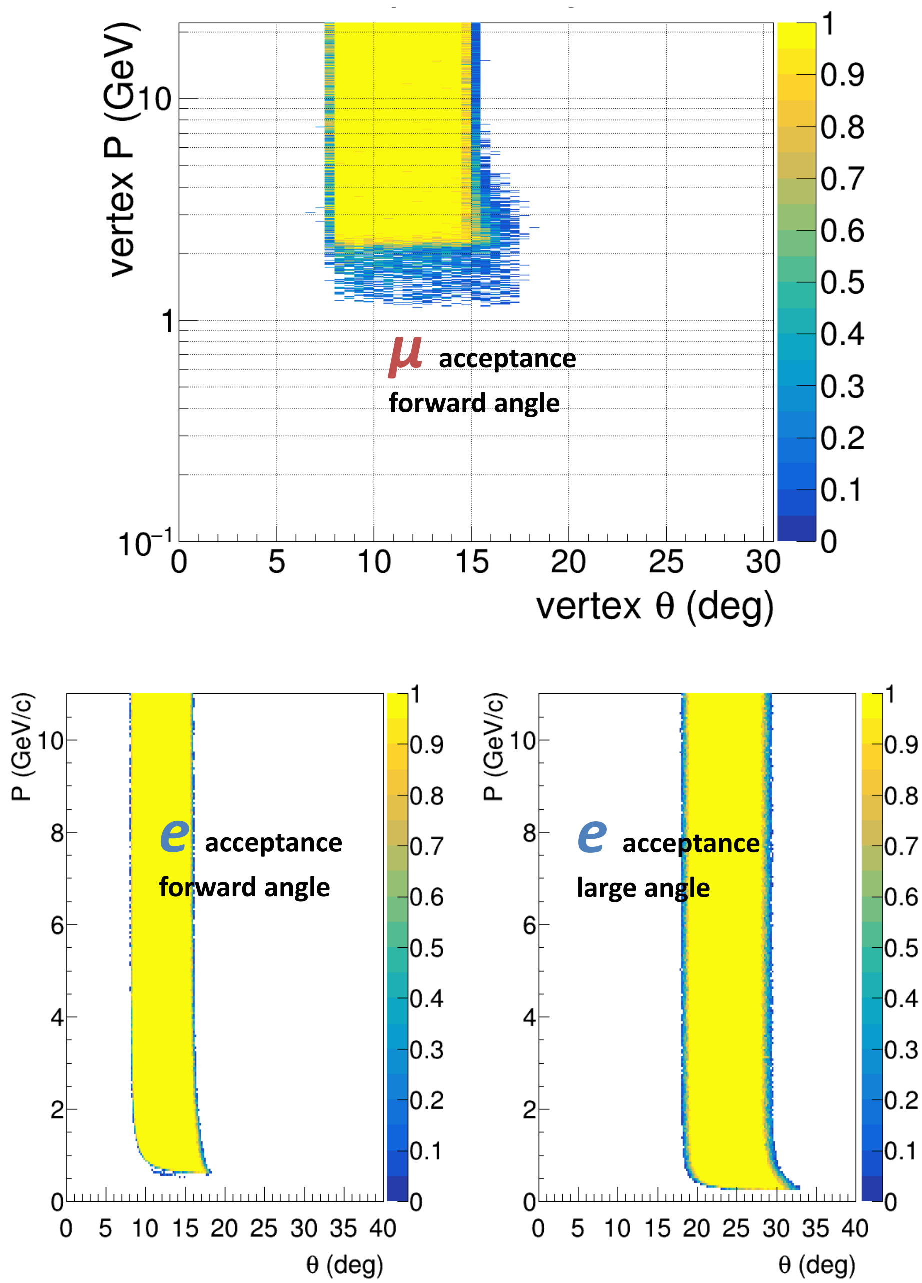

Figure 14: The acceptance for μ (top) at FAMD and e (bottom) at the SoLID forward angle and large angle detectors.

5.2 Kinematic coverage

Since the DDVCS events are always mixed with the Bethe-Heitler (BH) events with much large cross section, the physics rate estimation is simply based on the BH event generator "grape-dilepton" [67]. The program is widely used for various studies for ep scattering and its cross section calculation is based on exact matrix element in the electroweak theory at tree level. Please note "grape-dilepton" refers to Compton and BH process which are what we refer as BH_1 and BH_2 process as shown in Figure [?].

The results for 3 fold topology with proton not required is shown in polar angle and momentum at Figure 15 and various kinematic variables at Figure 16.

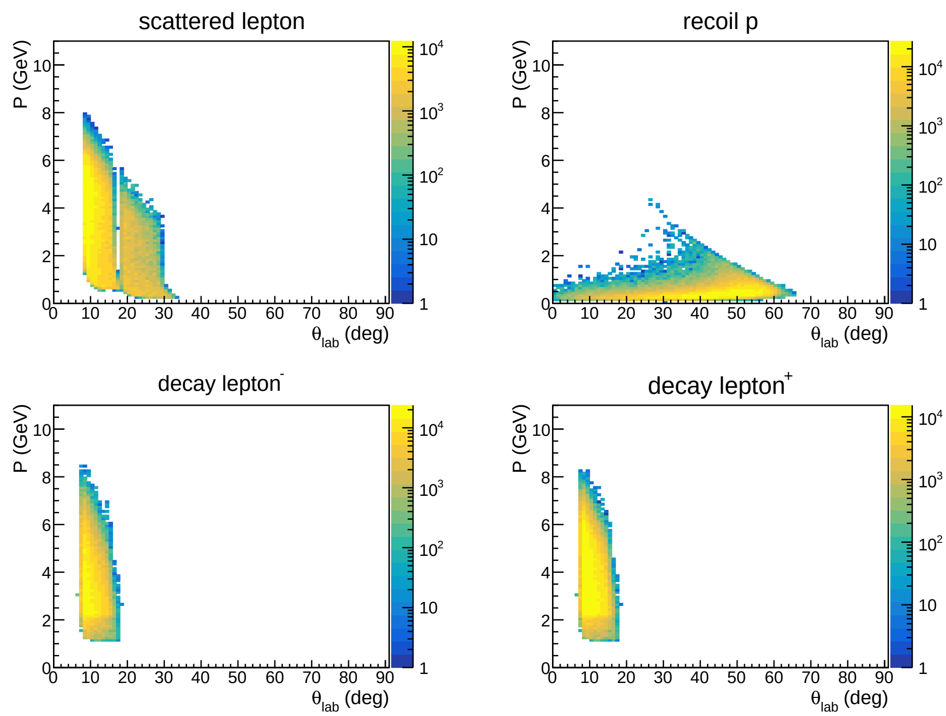

Figure 15: Momentum and polar angle distribution of BH 3 fold events

Using the luminosity $1.2 \times 10^{37}.cm^{-2}.s^{-1}$ and 100 days running time, it was determined that the total number of BH events has the muons pair invariant mass distribution shown in 17. There are about 2.8M 3 fold BH events detected and among them 1.3M events in the resonance free region (above the mass of 1.2 GeV) can be used for the physics analysis. A factorization cut like $-t < Q^2 + Q'^2$ would cut away a couple percent of events. With such high statistics, we can afford to bin data into multidimensional kinematic bins to measure asymmetries and compare to GPD models. 0.2M and 0.1M of 4 fold BH events will be detected for entire mass region and resonance free region as well. They can be used to check physics analysis process.

5.3 Event identification and exclusivity

Requiring 3 final state particles detected already makes the 3 fold BH events very clean. We can further ensure the exclusivity by exammining the missing mass of $(e\mu^+\mu^- X)$ for 3 fold BH events, where X should be at the proton mass for exclusive events with resolution determined by SoLID inner tracking (not the tackers in FAMD) which is close to the target and has no big multiple scattering. The SoLID inner tracking resolution was evaluated using the electron and proton momentum tracking resolution for the $Jpsi$ experiment. We use the proton resolution for muons and the estimation is conservative. Further we have added an additional 1.5 safety factor on all tracking resolution. The event generator “grape-dilepton” can produced both the elastic BH events which is what we want to detect and the quasi-elastic BH events which has additional pion or other particles produced. The initial radiation effect for 11 GeV electron beam is also turned on, Then we examine the missing mass distribution of the 3 fold toplogy for both types of events. Figure18 shows that SoLID tracking resolution is sufficient to have exclusive elastic BH events by putting a cut at 1.15 GeV. The quasi-elastic BH events contamination is only about 3-4% for the entire mass region or the resonance free region of $M_{\mu^+\mu^-}$.

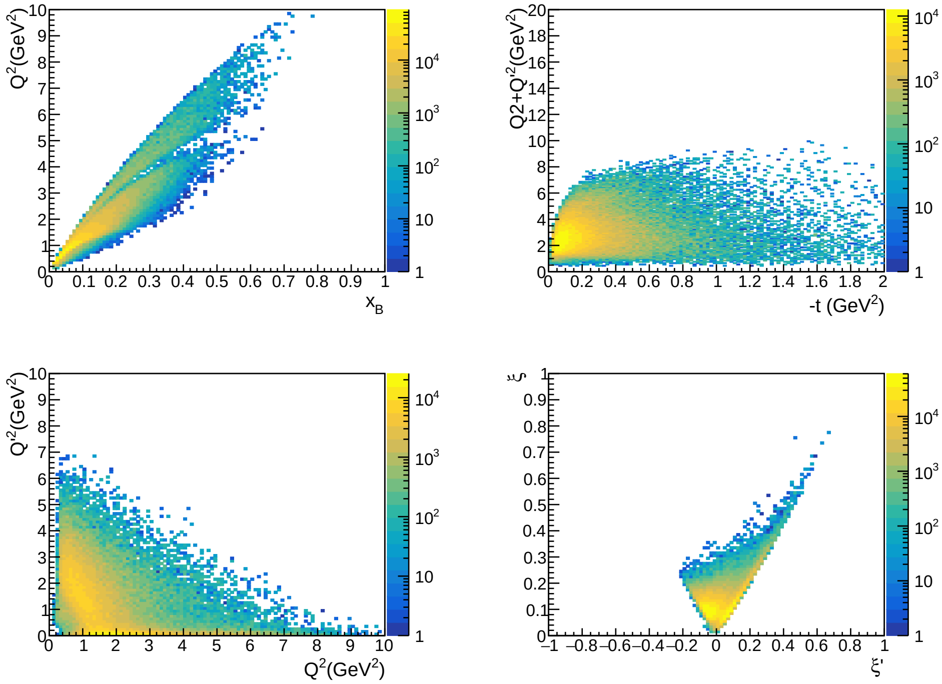

Figure 16: Kinematic distribution of BH 3 fold events

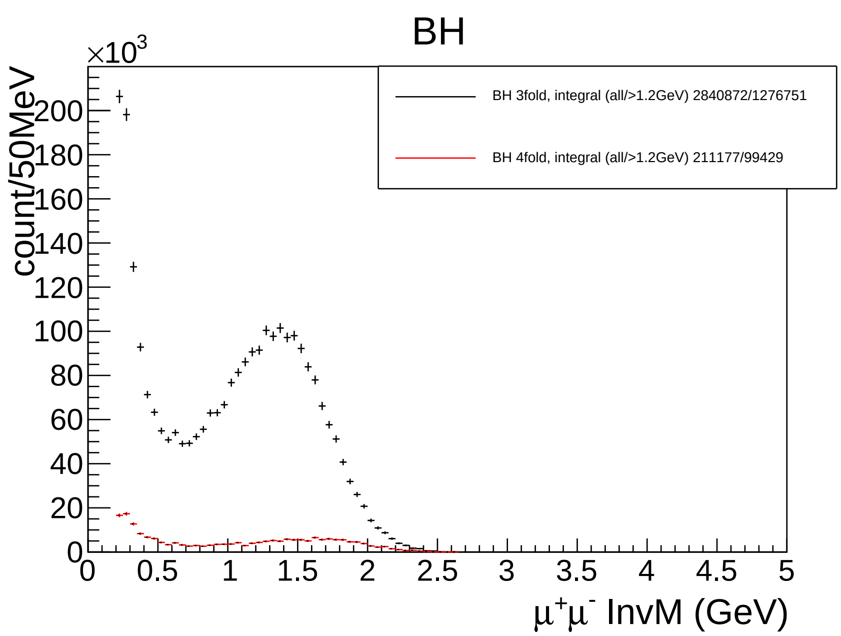

Figure 17: Total BH muons pairs with additional electron (3 fold) and additional electron and proton (4 fold) detected for the run time

5.4 Background

Extensive background studies were carried out for the J/ψ experiment and showed that SoLID could handle a luminosity of 1.2×10^{37} and the luminosity was chosen for optimal reconstruction of J/Psi events. The

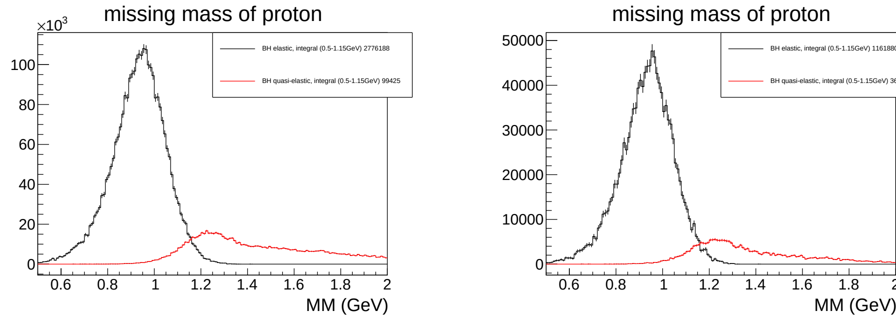

Figure 18: Missing mass distribution for 3 fold BH elastic (black) and quasi-elastic (red) events. The cut near missing mass 1.15 GeV can be used to separate the two type of events. The background quasi-elastic events only count about 3-4% of the signal elastic events for the entire range of $M_{\mu^+\mu^-}$ (left plot) and $M_{\mu^+\mu^-} > 1.2$ GeV region (right plot).

background for DDVCS inside of SoLID will be similar to the J/ψ experiment.

Our background study focus on the background in the forward angle muon detector using full Geant4 simulation and physics generators. The beam induced low energy background were evaluated with 11GeV electron beam shooting on the 15 cm long liquid hydrogen target and they are mostly contained within SoLID endcap and has negligible effect in the muon detector.

The main background for our measurement is from pions produced at the target. We present our simulation study for pion blocking and evaluate the remaining background in the following sections.

5.4.1 Pion blocking study

The initial pions from the target need to fly about 10 m before they reach FAMD and pass its 3 layers of irons. They can be blocked by the heavy materials along the way like ECAL and magnet iron. Some secondary pions can be generated during those hadronic interactions. And many of them decay into muons. The best way to suppress pions is to block them with a lot of heavy materials, but there are always small chances secondary pion and muon can go through.

A flat distribution of pions from the target location thrown into SoLIDμ setup in Geant4 is used to model pion blocking including its reaction with materials along its flight path and its muon decay. A pion from the target has a small chance of reaching the forward angle muon detector as pion, decay muon or other secondary charge particles. We call it the pion hit probability as shown in Fig. 19 for charge particle hits from the initial pion at 3 different layers of FAMD.

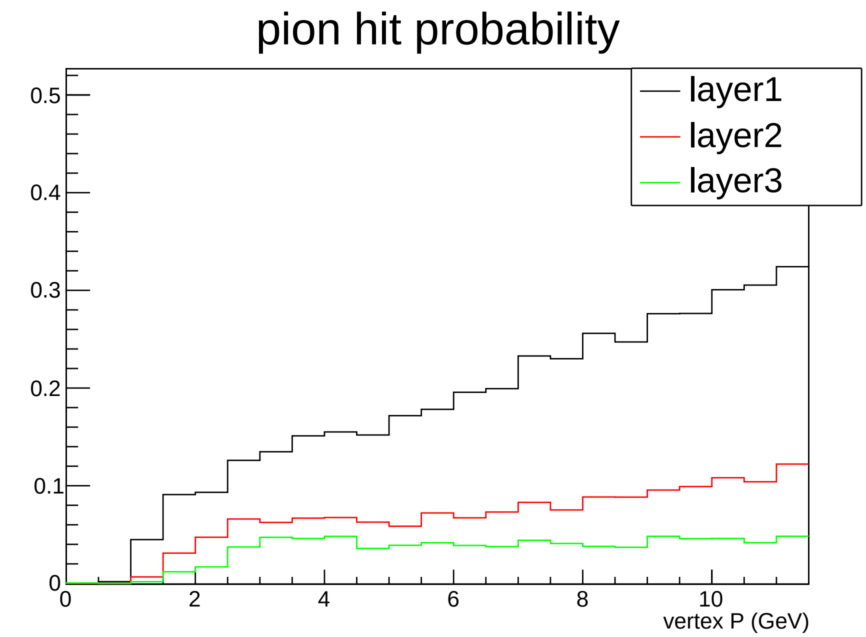

Figure 19: The pion hit probability at 3 layers subdetectors of FAMD is shown.

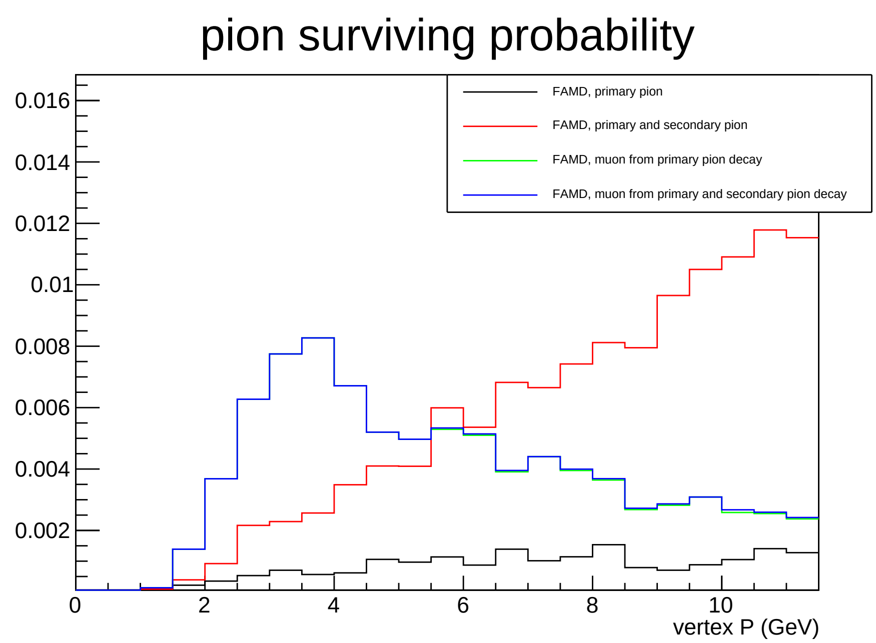

Figure 20: The pion surviving probability at FAMD is shown. The primary pions from the target can have 0.1% chance to survive, while secondary pions produced by primary pions along the way can have 1% percent. Muons are mostly from primary pions and have the probability of decaying and reaching the detector from 0.1% to 1%.

The aforementioned pion hit probability at FAMD considered all charged particles at FAMD from charged pions at the target. They are good to estimate the single particle rate at FAMD. But the offline muon construction from the target will need to consider both track reconstruction from the GEM trackers inside SoLID and FAMD response. From the same simulation study, we count the charged pion and muon at the layer3 of FAMD with a matching track at the GEM tracking planes inside SoLID and compare them to the initial pion from the target. We call it the pion surviving probability as shown in Fig. 20. A pion from the target has a small chance of reaching the back of FAMD as a primary pion, a secondary pion, or a decay muon from the two types of pions. Primary pions are the initial pion and has a survival chance of only 0.1%, while secondary pions produced by primary pions along the way can increase with momentum and reach 1.2% at 11 GeV/c. Those secondary pions can be further suppressed by cutting on their energy deposition in the scintillators of FAMD which generally have larger values than that of muons and primary pions behaving like minimum ionizing particles, as shown in the bottom left plot of Fig. 21. This is because the appearance of secondary pions at layer3 is an indication that most likely the initial pions have started showering in FAMD as in the top plot of Fig. 21. We give the suppression a conservative estimation as a factor of 2. Additional transverse energy deposition distribution could be used to further enhance the suppression. Comparing to secondary pions, muons from pion decay can have a maximum of 0.8% surviving probability near 4 GeV/c. They are mostly from primary pion decay instead of secondary pions and their behavivor in FAMD is just like muons from the target. The main differenence is their vertex are distributed along the 10 m flight path instead from the target only as shown in the bottom left plot of Fig. 21. We could potentially use vertex cut from tracking to suppress muons from pion decay. But it's not an easy task because those muons tend to fly in the same direction of decaying pions which will make its vertex determination difficult. To be conservative, we didn't apply any suppression on them. In summary, those pion surviving probabilities with a additional factor 2 secondary pion suppression can help us estimate the final reconstructed background particles from pions produced at the target, while our signal particles are muons from the target.

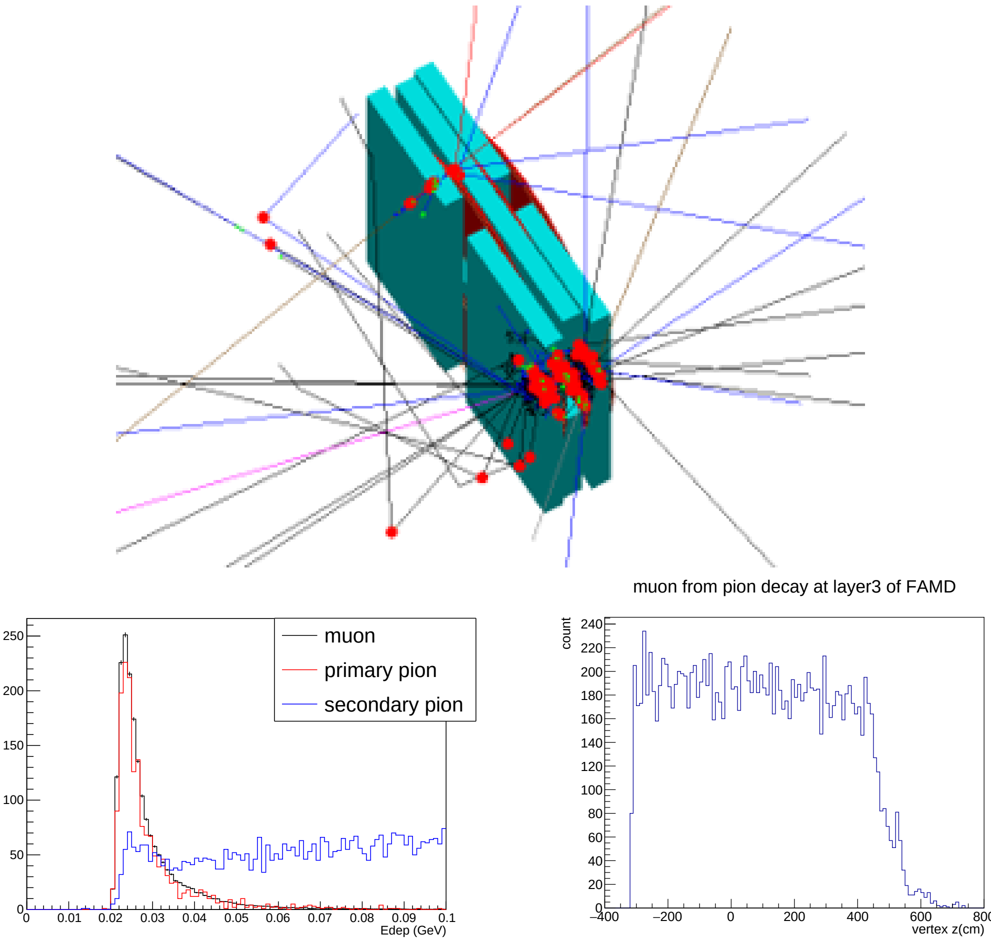

Figure 21: Top plot: Geant4 simulation of a muon hitting the left side FAMD with less hits and less energy deposition and a pion hitting the right side with more hits and more energy deposition. Lower left plot: Total energy deposition in 3 layers of scintilators in FAMD for muons, primary pions and secondary pions which has passed through all 3 layers. Lower right plot: pions from the target decay into muons and then pass FAMD. Those muon from pion decay have vertex z along the flight path.

5.4.2 Single pion background

The single pion rate from the LH2 target was evaluated by using the "evgen_bggen" event generator [68]. which combines PYTHIA event generator with resonance models for electroproduction. It was used for Hall D and SoLID study and compared to data.

Combining "evgen_bggen" output with the pion hit probability, we obtained the single particle rate at the forward muon detector. Their rate distribution over polar angle and momentum for 3 layers are shown in Figure 22. The integrated rate of negative pion is 616/285/154 khz at layer1/2/3. And the integrated rate of positive pion is 605/281/153 khz at layer1/2/3. So the total rate is about 1221/566/311 khz at layer1/2/3. From the same study, we also obtain the rate per area distributions shown in Figure 23. The combined max rate per area is about 16/8/4 Hz/cm^2 at the most inner radius of layer1/2/3 . We do not expect any issue operating μRWell/GEM trackers which can handle 100-1000kHz/cm^2 easily or scitilators with proper segmention.

Our main trigger will be the coincidence trigger requiring two single charge particle at the layer3 of the forward angle muon detector. Considering the total single particle rate there 311 khz, we add a safety factor 2 to make it 600 khz. Then using 50 ns coincidence timing window, the coincidence trigger rate can be estimated to be 20 kHz.

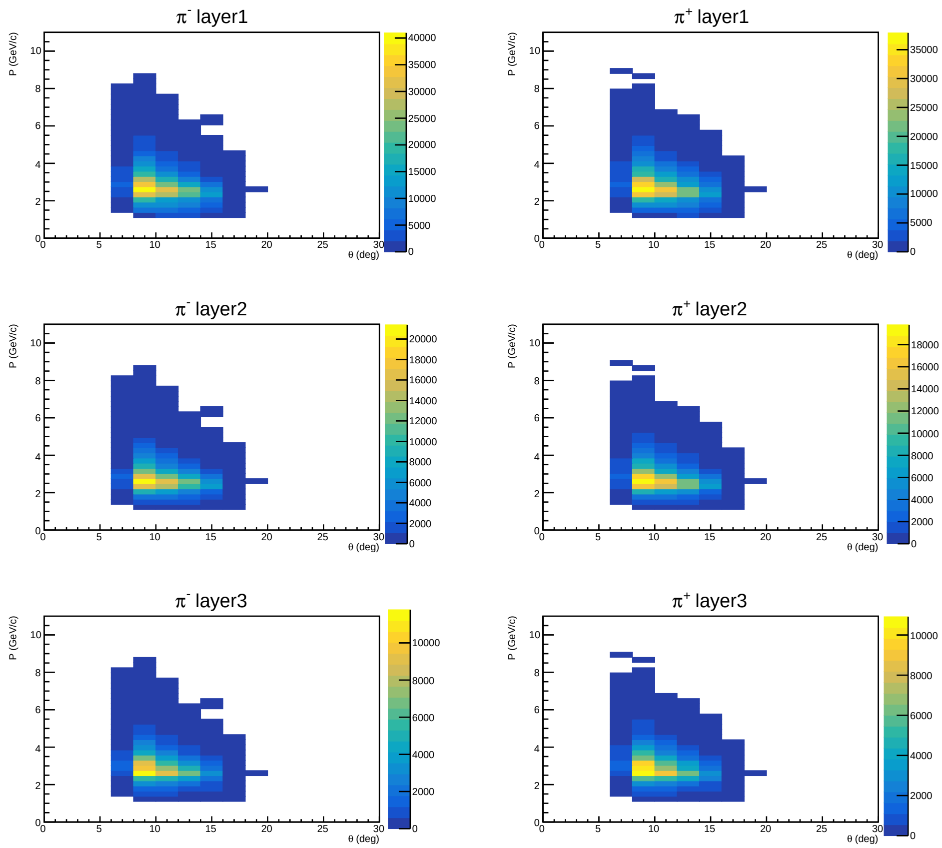

Figure 22: Single particle rate at layer1 (top),layer2 (middle),layer3 (bottom) of FAMD. They are from negative pion (left) or positive pion (right) produced at the target.

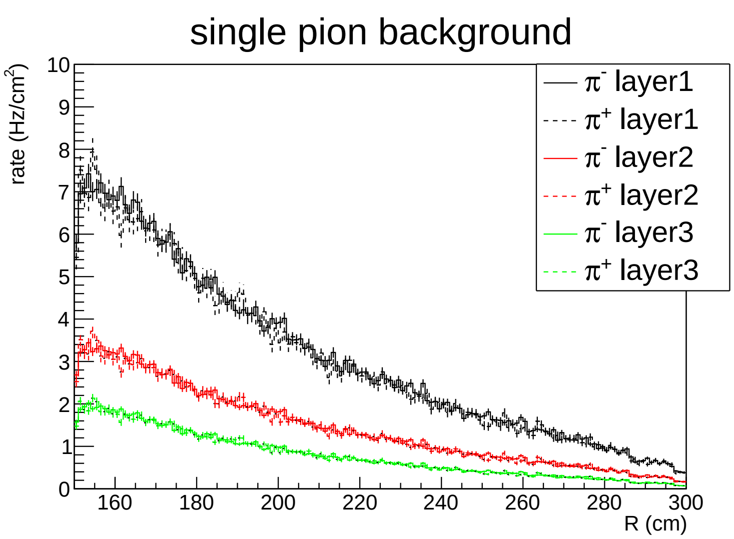

Figure 23: Single particle rate per area at layer1 (top),layer2 (middle),layer3 (bottom) of FAMD. They are from negative pion or positive pion produced at the target.

5.4.3 Two pion exclusive background

Because we will always require at least 3 particles in the final state including the scattered electron, and two muon candidates. The main background for the offline analysis is the two pion exclusive channels (2pi). It will pass the two charge particle coincidence trigger in the muon detector and survive the missing proton mass exclusivity cut because muon and pion masses are very close. We used the event generator "twopeg" [69] to study the channel $e^-p \to e^-p\pi^+\pi^-$. It includes both resonance and non-resonance regions and fits the five-fold differential structure functions from the recent versions of the JM model to all results on charged double pion photo- and electroproduction cross sections from CLAS 6GeV. To estimate the cross sections in the regions not covered by 6 GeV data, a specialized extrapolation is used to extend the coverage to 12 GeV beam to cover in W from the reaction threshold up to 4.5 GeV and the result were compared to 12 GeV data.

Combining the "twopeg" generator and the pion surviving probabilities with additional factor 2 on the sceondary pions, we obtained the counts from the two pion exclusive channels as shown in Figure 24. The results are separated into the cases for neither pion decays, negative pion decays into muon, positive pion decays into muon, and both pions decay into muons. The first 3 cases have smaller counts because of the strong pion blocking. The total counts from the 2pi channel are about 7% of the BH muon counts for the entire mass range and 5% for the region $M_{\mu\mu} > 1.2$ GeV. More detailed study of FAMD response and tracking with vertex cuts could suppress the 2pi background further. In addition, the two pion exclusive channel which should have no asymmetry, will also be measured by the SoLID main detectors with high precision to help control its systematics.

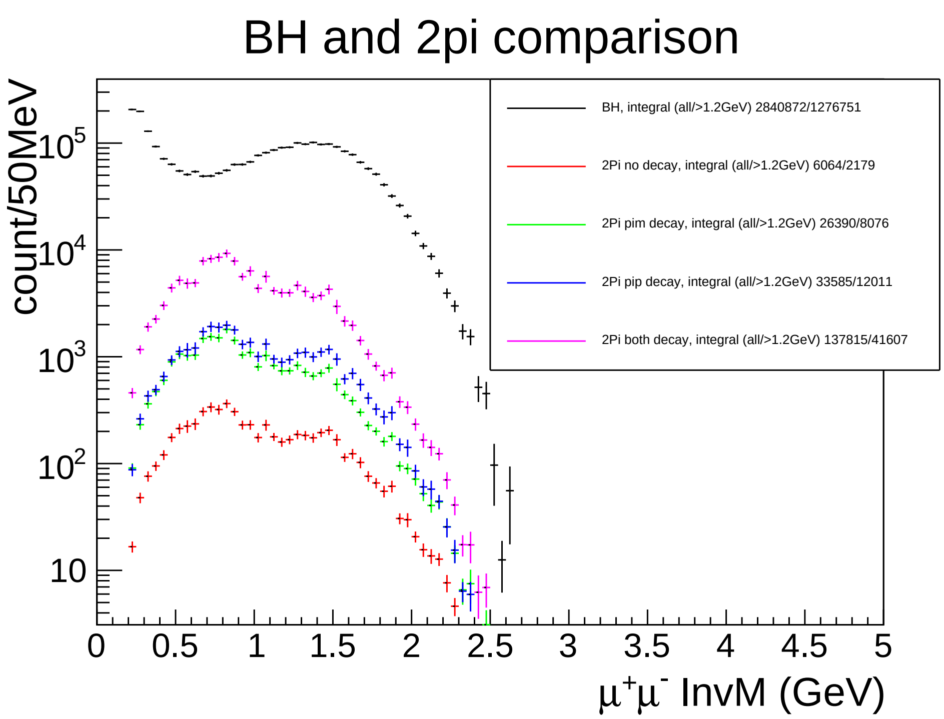

Figure 24: Beside BH counts from grape, the two pion exclusive channel contamination are shown in 4 cases, neither pion decay, negative pion decays into muon, positive pion decays into muon, and both pions decay. The counts for all events and events after the cut of two muon invariant mass larger than 1.2 GeV are shown,

6 Projected results

Experimental projections were built on the VGG and GK19 model predictions while counting rates from the realistic simulation described in section 5. DDVCS event selection is determined by detecting the scattered electron and the produced muon pairs. Proton-detected detection topology has not been taken into account. Detection is established by the SoLID DDVCS acceptance maps of Fig. 14 and an overall 70% reconstruction efficiency. Finally, the $e\mu^+\mu^-(N)$ event count is obtained by re-scaling the acceptance-filtered events accordingly to the expected luminosity of 1.2×10^{37} cm$^{-2} \cdot$s^{-1} and 100 days of beam time. A detailed description of the binning scheme and the full set of experimental projections is shown in section 6.3.

To explore the physics reach of the SoLID detector, we consider the equal-number-of-events binning scheme shown in Fig. 25. The binning was defined over the $(\xi', \xi, t, \varphi_\mu)$ phase space as it is directly related to the CFF/GPD phase space, which we ultimately intend to explore. Initially, we define ten bins in the (ξ', ξ) space, followed by three bins in t. Thirty bins were defined in total. Given the expected statistics, data allows a four-dimensional exploration of the DDVCS phase space to access CFFs through precise BSA and muon Charge Asymmetries (μCA). As the factorization scale is given by $Q^2 + Q'^2$ and we are accessing small Q^2 values, we can neglect in a first approximation the Q^2 dependence of GPDs. Therefore, it is possible to explore the three-dimensional phase space of CFFs with the foreseen data.

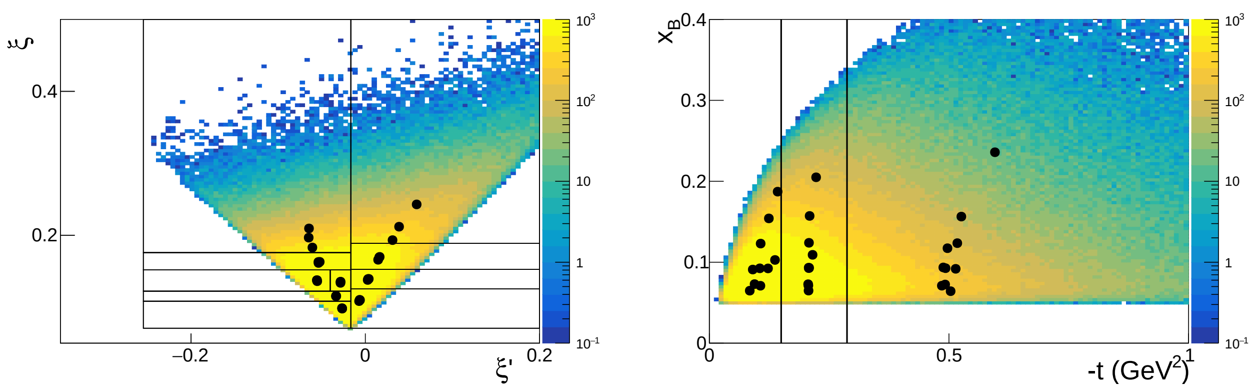

(a) (ξ', ξ) space. (b) $(-t, x_B)$ space.

Figure 25: DDVCS Kinematic reach of the SoLID detector and binning scheme used for experimental projections. Points represent the mean kinematic values over the five-dimensional binning scheme.

6.1 Beam spin asymmetry

Given the Beam Spin Asymmetry (BSA) prediction A_{LU} given by the GK19 model and the simulated dataset's event rate estimate N, the BSA statistical error bar is computed as

$$\Delta A_{LU}^{stat} = \sqrt{\frac{1 - (A_{LU}/P)^2}{N}}, \tag{44}$$

where $P = (86 \pm 1)\%$ is the polarization of the expected electron beam for SoLID. The systematic error due to the beam polarization is also included in the BSA error estimate by quadratically adding it to the statistical error as:

$$\Delta A_{LU} = \sqrt{(\Delta A_{LU}^{stat})^2 + \left(A_{LU}\frac{\Delta P}{P}\right)^2}. \tag{45}$$

Statistical fluctuations are introduced by shuffling the model-predicted A_{LU} value following a Gaussian distribution centered at A_{LU} and standard deviation ΔA_{LU} ($A_{LU} \to \mathcal{G}(A_{LU}, \Delta A_{LU})$).

As shown in Fig. 25, the SoLID detector would mainly access the TCS-like region of the DDVCS phase space ($\xi' < 0$). Contrary to DVCS, the factorization condition $Q^2 + Q'^2 > 1$ GeV^2 let us include in the analysis low Q^2 events for large enough Q'^2. In particular, we select the $Q'^2 > 1.4$ GeV^2 region, excluding the main vector meson resonances in the spectrum, while Q^2 reaches values as small as 0.2 GeV^2 given by the electron acceptance. The access to the DVCS-Like region ($\xi' > 0$) is therefore subject to the condition $Q^2 > Q'^2 > 1.4$ GeV^2, which is difficult to achieve with an 11 GeV beam. Nevertheless, the SoLID detector could provide exploratory measurements in the DVCS-like region. Fig. 26 shows the integrated BSA prediction on the DVCS-like region, while the set of projected measurements in both TCS- and DVCS-like regions is shown in section 6.3. The latter indicates that the SoLID detector will allow a first-time observation of the asymmetry sign change when transitioning between the DVCS- and TCS-like regions.

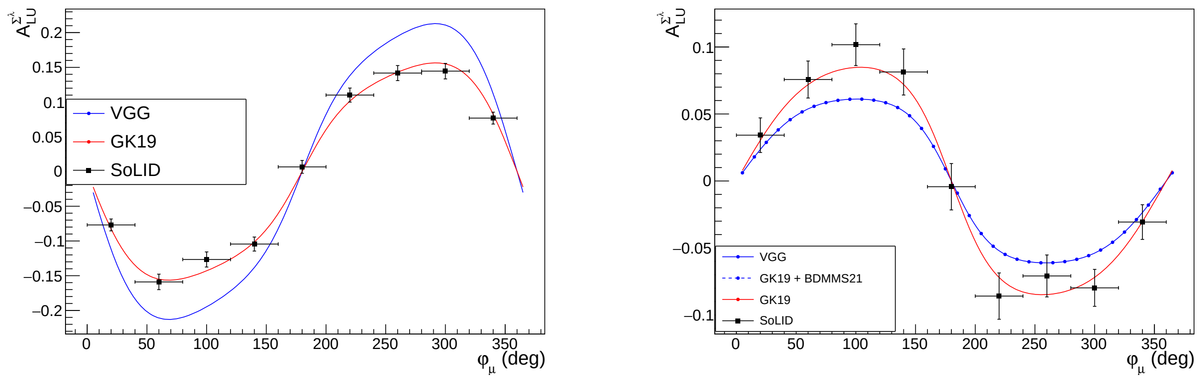

(a) BSA in the TCS-like region (Bin 21).

(b) Integrated BSA in the DVCS-like region.

Figure 26: Sample BSA projections

It is crucial to notice that the BSA is presented as a function of φ_μ, i.e. using the 5-fold differential cross-section Σ^λ obtained when integrating over ϕ and θ_l as defined in Eq. 27. Although a BSA constructed with σ^λ accesses the same CFF information, the kinematic factors entering the calculation can suppress or enhance the asymmetry amplitude at a given kinematics. In particular, the integrated Σ^λ cross-section amplifies the observables on the TCS-like region while suppressing them on the DVCS-like region. The opposite holds for σ^λ. As a result, the BSA is furnished with large amplitudes, as shown in Fig. 26. All BSA projections can be consulted in section 6.3. While the results show feasible measurements in most bins, some projections present large error bars compared to the asymmetry amplitude. The latter corresponds to bins of significant statistics. Still, small ξ', thus justifying the small asymmetry amplitude as it is predicted to decrease when ξ' approaches zero, vanish, and change sign accordingly with ξ'.

Let us also consider two bins in ξ' at relatively large ξ given by $0.3 < \xi < 0.4$, being 0.4 the upper limit of the ξ SoLID acceptance, and integrated over all other variables. The BSA associated with such kinematics is shown in Fig. 27 according to the GK19 model and the GK19 + BDMMS21 model, being the latter a shadow GPD model [63]. Given the foreseen kinematic reach of the SoLID detector, the experimental projection points to a first-time exploratory measurement constraining shadow GPD models.

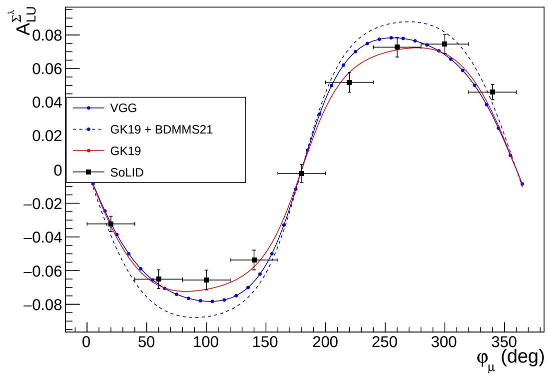

(a) $-0.1 < \xi' < -0.04$.

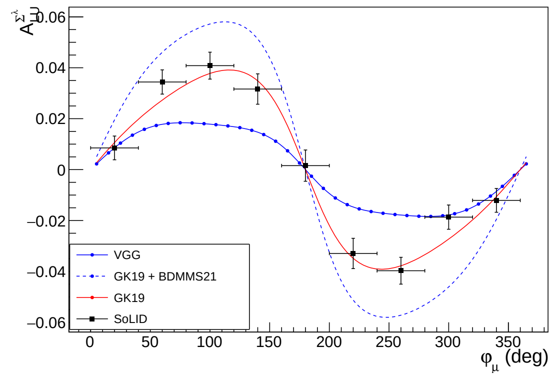

(b) $-0.04 < \xi' < 0.1$.

Figure 27: Projected exploratory BSA measurements sensitive to shadow GPDs in the $0.3 < \xi < 0.4$ region.

In brief, the experiment covers a broad kinematic range enriched by the $-t \ll Q^2 + Q'^2$ condition, allowing the measurement of low Q^2 events. As a result, the DDVCS reaction can be studied on a four-dimensional grid, with $(\xi', \xi, t, \varphi_\mu)$ a preliminary choice of binning to be optimized for experimental data. In particular, BSA measurements over such a kinematic grid would allow to constrain GPDs in uncharted territories as they access the singlet GPD combination contained in the imaginary part of CFFs. Moreover, the SoLID experimental program would allow a first-time observation of the GPD sign difference in the TCS- and DVCS-like regions and shadow-GPD-sensitive measurements. The expected experimental signals enable a meaningful extraction of the CFFs from the φ_μ-modulation, thus providing invaluable constraints for GPDs through global fit methods.

6.2 Muon charge asymmetry μCA

Following the discussion of 2.2.3, charge conjugation asymmetries are accessible with the DDVCS process as opposite-charge states are found in the lepton pair. Thus reducing the sources of systematic uncertainties entering into a Beam Charge Asymmetry with electron and positron beams. Similar to BSA projections, given the theory prediction $A_{UU}^{\mu^\pm}$ as of the GK19 model and the simulated dataset's event rate estimate N, the statistical error bar for the muon-charge (Forward-Backward) asymmetry (μCA) is given by:

$$(\Delta A_{UU}^{\mu^\pm})^{stat} = \sqrt{\frac{1 - (A_{UU}^{\mu^\pm})^2}{N}}. \tag{46}$$

The μCA, as defined in Eq. (32), receives its main contributions from the $\cos(\varphi_\mu)$ and $\cos(3\varphi_\mu)$ terms. The latter is a consequence of the $P_3P_4(\theta_\mu, \varphi_\mu)$ propagators in the BH_{12} and $\mathcal{I}_2^\lambda$ terms of the unpolarized cross-section, in Eqs. (20) and (15) respectively. Fig. 28 shows two examples of the projected μCA. On the one hand, model predictions are similar and point to large asymmetry amplitudes that can be measured with the SoLID detector. Therefore, accessing the real part of CFFs out of the $\xi = \pm\xi'$ trajectory as in DVCS and TCS. On the other hand, Fig. 28 shows that the $\cos(3\varphi)$ modulation might play a major role in some kinematics while being negligible in others. As the asymmetry accesses the interference between the DDVCS and BH_2 components of the cross-section, both cosine moments would provide valuable information on CFFs. Given the expected statistics, only the extraction of the $\cos\varphi$ moment is foreseen.

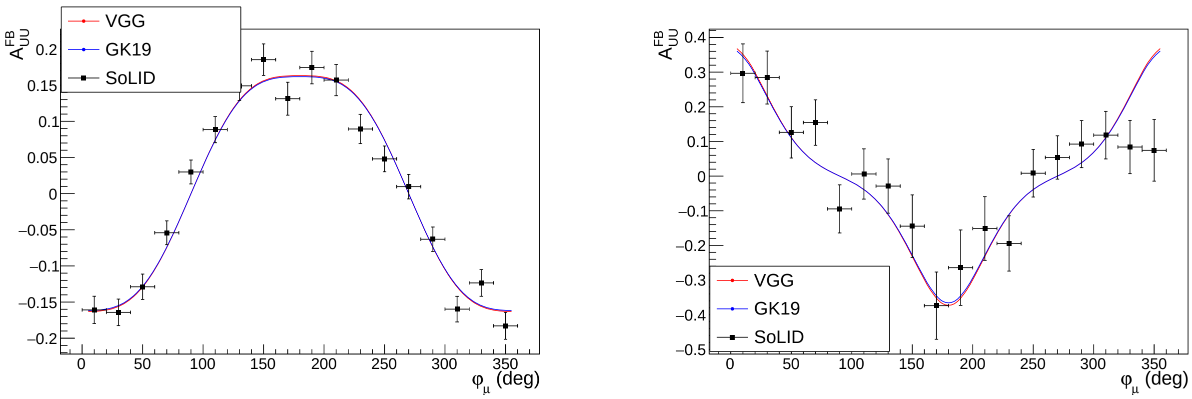

(a) bin 24.

(b) bin 7.

Figure 28: Sample μCA asymmetry projections.

To study the feasibility of the cosine moments and determine the expected statistical errors of its extraction, we perform a fit to the experimental projection to the function:

$$A_{UU}^{FB} = a_0 + a_1 \cos(\varphi) + a_3 \cos(3\varphi), \tag{47}$$

where the coefficients a_k are given by the sum of the VCS$\cdot$BH$_2$ and BH$_1\cdot$BH$_2$ components as $a_k = a_k^{VCS\cdot BH_2} + a_k^{BH_1\cdot BH_2}$. Such fit is performed ten thousand times, shuffling the projected asymmetries on each iteration and collecting the b_1 parameter to construct its statistics. Fig. 29 shows the example of bin 13, where the BH contribution is relatively small and allows for a $\cos\varphi_\mu$ extraction within a 7.5% error given by the standard deviation of the $\Delta a_1 = a_1^{fit} - a_1^{gen}$ distribution. The corresponding generated values are $a_1^{VCS\cdot BH_2} = 0.1364951$ and $a_1^{BH_1\cdot BH_2} = 0.0667959$. Therefore, the extraction of the $a_1^{VCS\cdot BH_2}$ moment is tied to a 11.1% statistical error. Likewise, it is obtained that a $\cos\varphi$ moment extraction can be obtained with an error smaller or equal to 30% in 13 out of the 30 defined kinematic bins.

Overall, we can conclude that the DDVCS μCA can be measured with the SoLID detector within 100 days of beam time. Such measurements are exploratory and provide access to the real part of CFFs over the non-explored regions of the GPD phase space subject to a suitable control of the systematic errors involved in the extraction procedure.

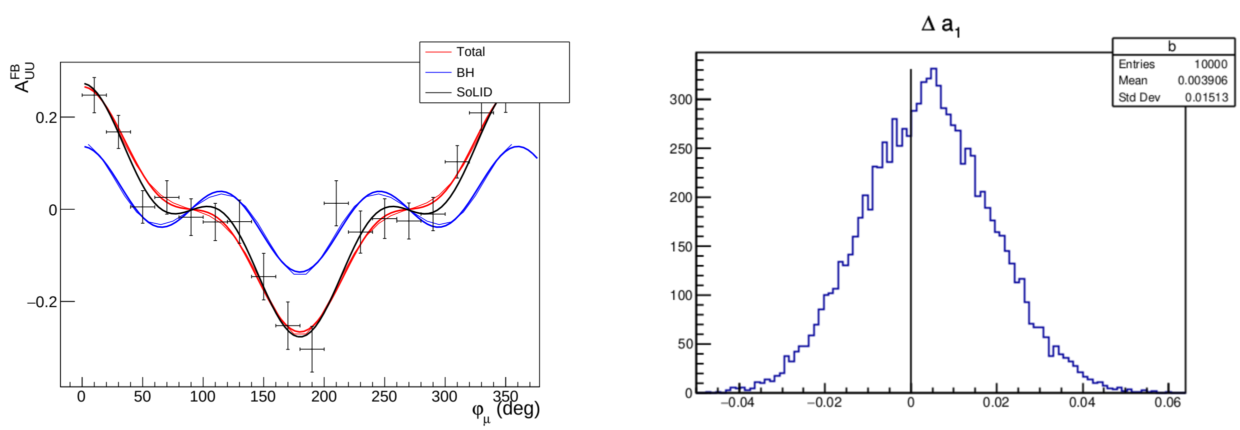

(a) μCA and the components entering the $\cos\varphi_\mu$ moment.

(b) Distribution of the $\cos\varphi_\mu$ moment of the μCA after 10k iterations.

Figure 29: Extraction of $\cos\varphi_\mu$ moment of the μCA on bin 13.

6.3 Complete set of experimental projections

In the following, we present the boundaries of the chosen binning scheme and the set of all experimental projections for the BSAs and μCAs.

Bin	ξ' range	ξ range	t range (GeV^2)
1	$-0.255 < \xi' < -0.017$	$0.152 < \xi < 0.176$	$-5.541 < t < -0.287$
2			$-0.287 < t < -0.150$
3			$-0.150 < t < -0.020$
4		$0.176 < \xi < 0.739$	$-5.541 < t < -0.287$
5			$-0.287 < t < -0.150$
6			$-0.150 < t < -0.020$
7	$-0.017 < \xi' < 0.512$	$0.071 < \xi < 0.126$	$-5.541 < t < -0.287$
8			$-0.287 < t < -0.150$
9			$-0.150 < t < -0.020$
10		$0.126 < \xi < 0.153$	$-5.541 < t < -0.287$
11			$-0.287 < t < -0.150$
12			$-0.150 < t < -0.020$
13		$0.153 < \xi < 0.189$	$-5.541 < t < -0.287$
14			$-0.287 < t < -0.150$
15			$-0.150 < t < -0.020$
16		$0.189 < \xi < 0.739$	$-5.541 < t < -0.287$
17			$-0.287 < t < -0.150$
18			$-0.150 < t < -0.020$
19	$-0.255 < \xi' < -0.017$	$0.071 < \xi < 0.108$	$-5.541 < t < -0.287$
20			$-0.287 < t < -0.150$
21			$-0.150 < t < -0.020$
22		$0.108 < \xi < 0.122$	$-5.541 < t < -0.287$
23			$-0.287 < t < -0.150$
24			$-0.150 < t < -0.020$
25	$-0.255 < \xi' < -0.040$	$0.122 < \xi < 0.152$	$-5.541 < t < -0.287$
26			$-0.287 < t < -0.150$
27			$-0.150 < t < -0.020$
28	$-0.040 < \xi' < -0.017$	$0.122 < \xi < 0.152$	$-5.541 < t < -0.287$
29			$-0.287 < t < -0.150$
30			$-0.150 < t < -0.020$

Table 1: Bin boundaries of the binning scheme shown in Fig. 25.

7 Control of systematics effects

Systematics effects on the measurement of BSAs and μCAs originate essentially from the detection of the reaction products that are the scattered electron and the dimuon-pair.

Whenever BSAs are defined at the level of the elementary cross section, as for DVCS and TCS, detector effects factorize on the numerator and on the denominator and finally cancel-out. In the DDVCS case, the smallness of the cross section does not make possible the consideration of BSAs at the 7-fold differential cross section level. It is mandatory to integrate over the angular distribution of the reaction products to allow the determination of BSAs at the 5-fold differential cross section level. As defined from Eqs. (29) and (30) and Eqs. (25) and (27), DDVCS BSAs remain sensitive to detector effects through the detection efficiency and effective acceptance of the SoLIDμ spectrometer for each particle.

more content will be added

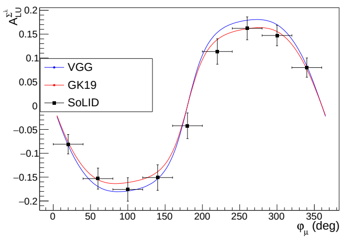

(a) Bin 1.

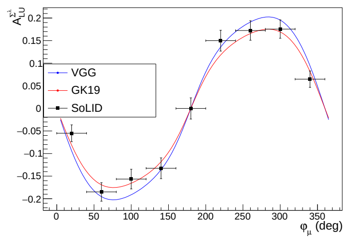

(b) Bin 2.

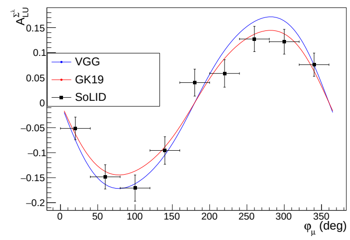

(c) Bin 3.

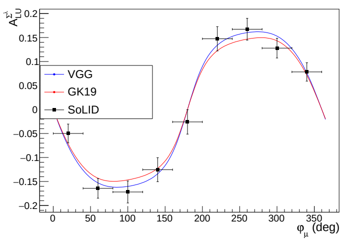

(d) Bin 4.

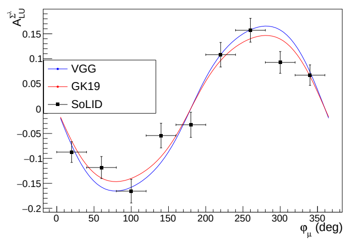

(e) Bin 5.

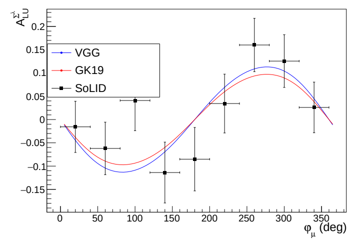

(f) Bin 6.

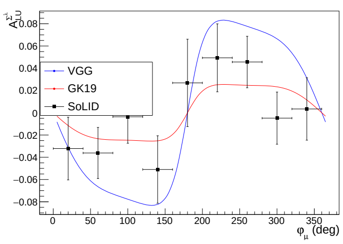

(g) Bin 7.

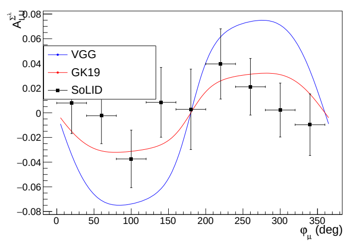

(h) Bin 8.

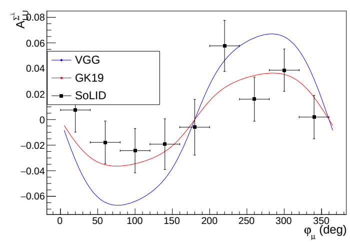

(i) Bin 9.

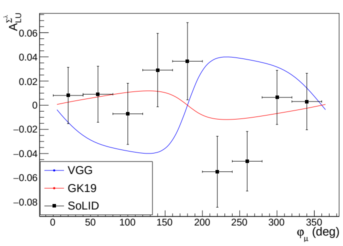

(j) Bin 10.

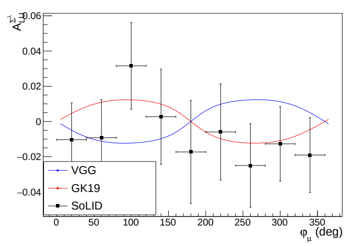

(k) Bin 11.

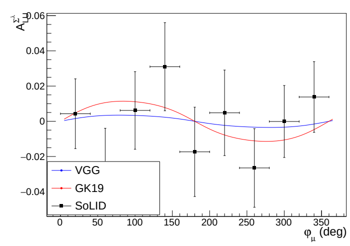

(l) Bin 12.

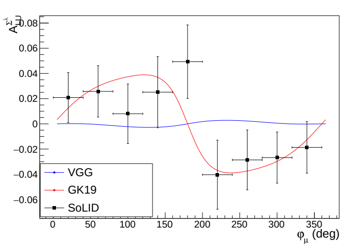

(m) Bin 13.

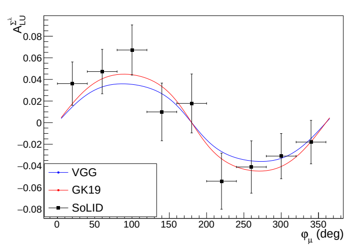

(n) Bin 14.

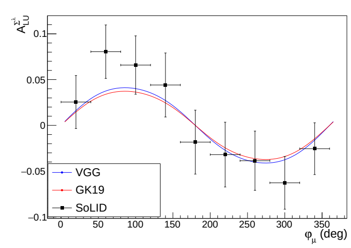

(o) Bin 15.

Figure 30: Set of all BSA experimental projections (1/2).

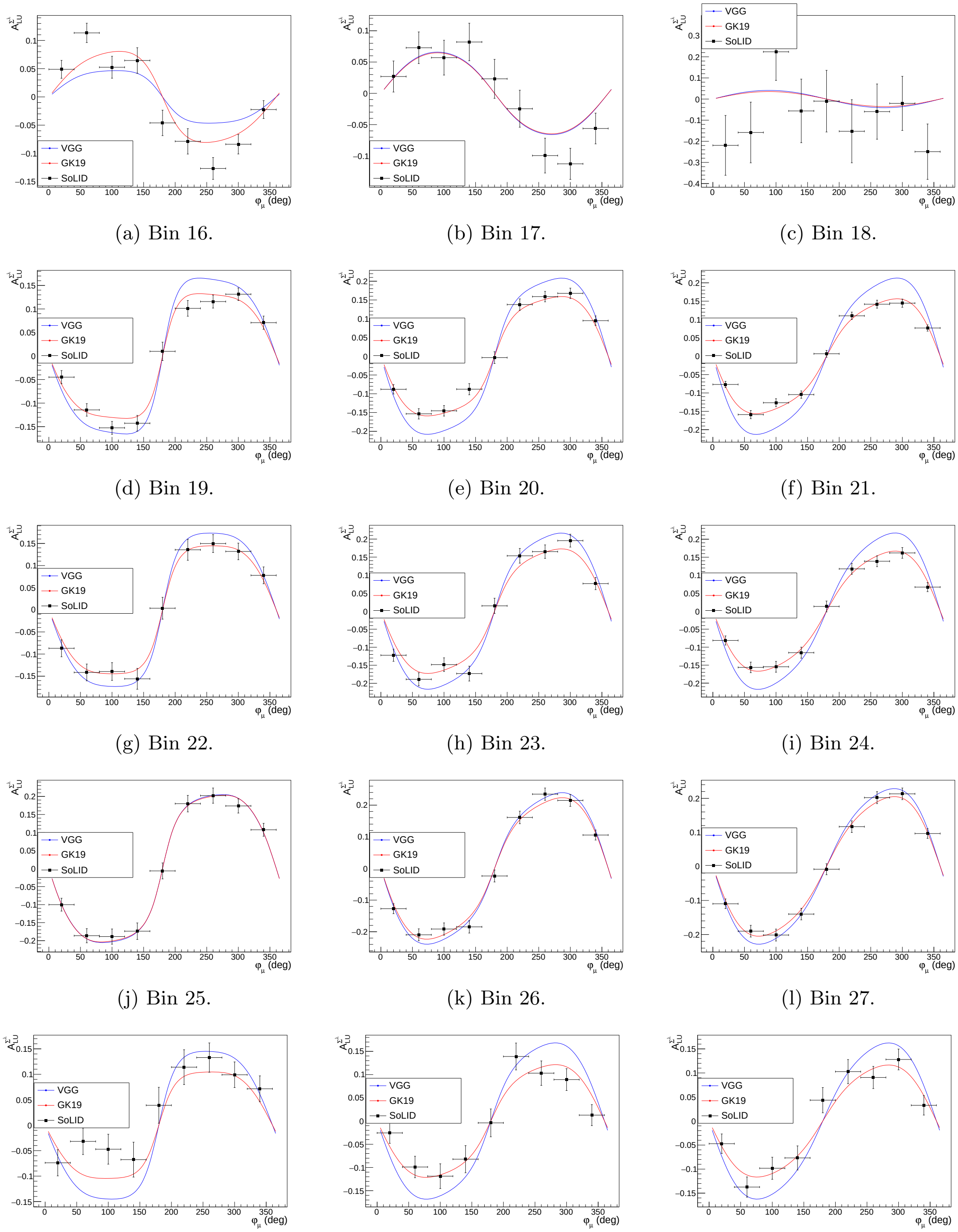

(a) Bin 16. (b) Bin 17. (c) Bin 18.

(d) Bin 19. (e) Bin 20. (f) Bin 21.

(g) Bin 22. (h) Bin 23. (i) Bin 24.

(j) Bin 25. (k) Bin 26. (l) Bin 27.

(m) Bin 28. (n) Bin 29. (o) Bin 30.

Figure 31: Set of all BSA experimental projections (2/2).

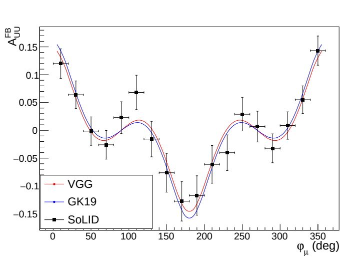

(a) Bin 1.

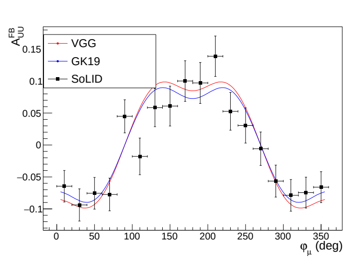

(b) Bin 2.

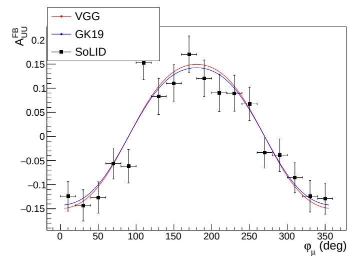

(c) Bin 3.

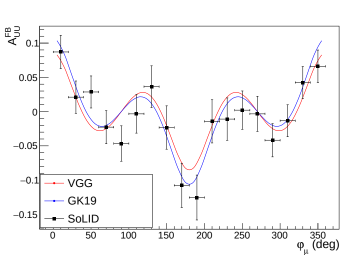

(d) Bin 4.

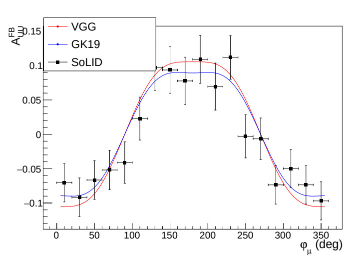

(e) Bin 5.

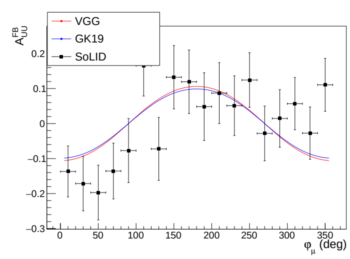

(f) Bin 6.

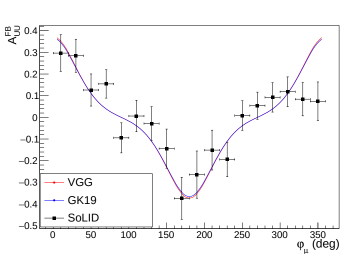

(g) Bin 7.

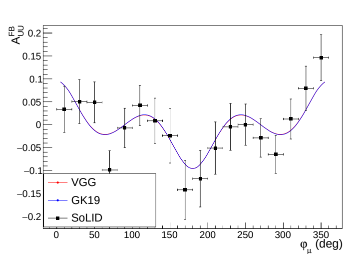

(h) Bin 8.

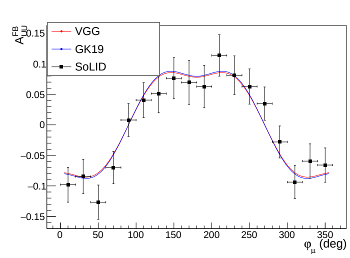

(i) Bin 9.

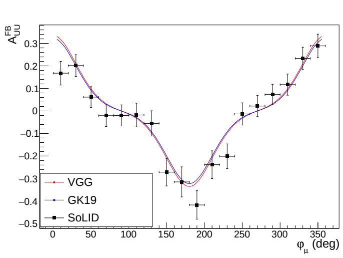

(j) Bin 10.

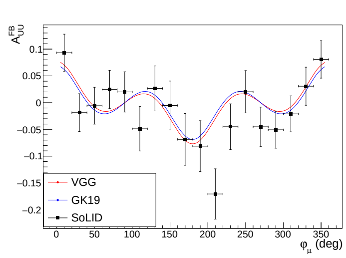

(k) Bin 11.

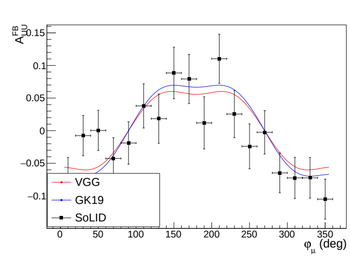

(l) Bin 12.

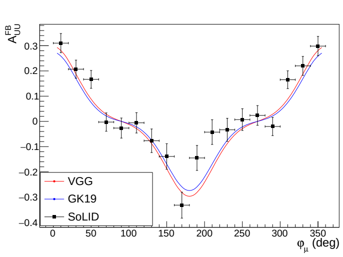

(m) Bin 13.

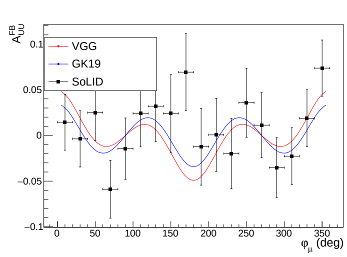

(n) Bin 14.

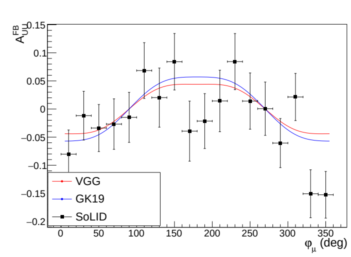

(o) Bin 15.

Figure 32: Set of all μCA experimental projections (1/2).

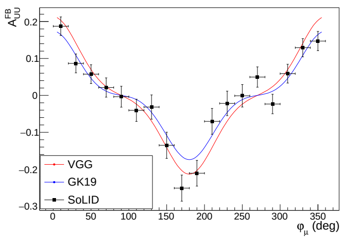

(a) Bin 16.

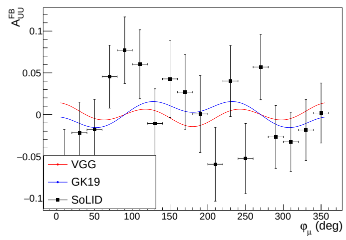

(b) Bin 17.

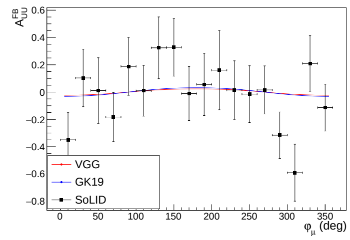

(c) Bin 18.

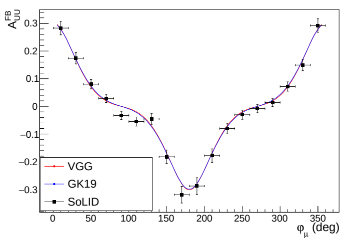

(d) Bin 19.

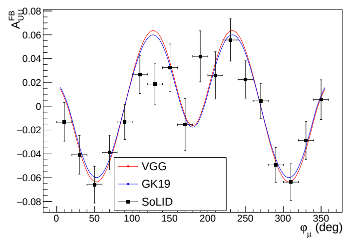

(e) Bin 20.

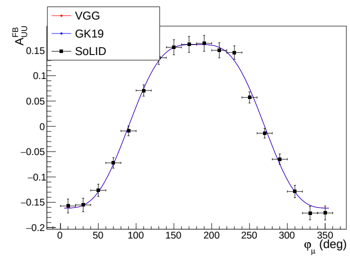

(f) Bin 21.

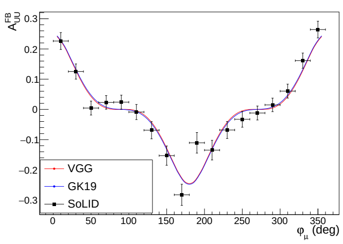

(g) Bin 22.

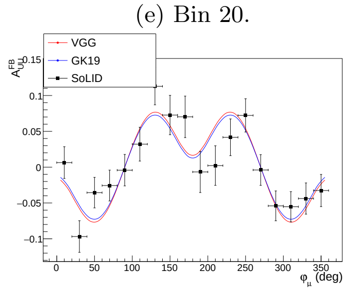

(h) Bin 23.

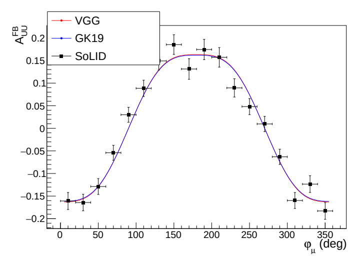

(i) Bin 24.

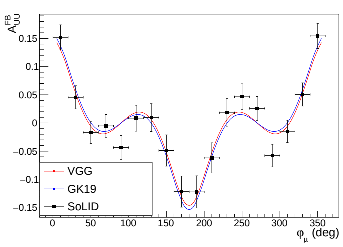

(j) Bin 25.

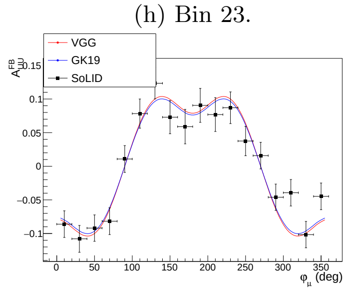

(k) Bin 26.

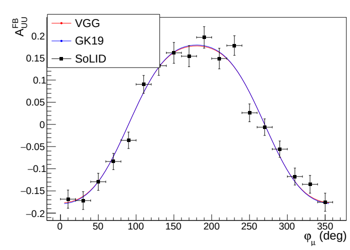

(l) Bin 27.

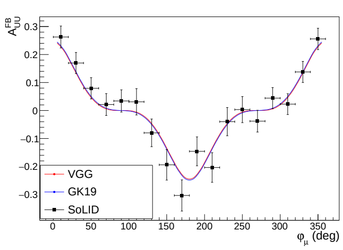

(m) Bin 28.

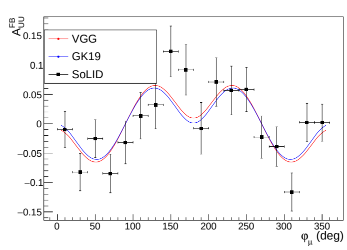

(n) Bin 29.

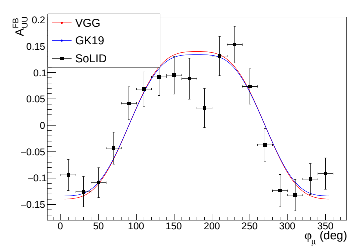

(o) Bin 30.

Figure 33: Set of all μCA experimental projections (2/2).

8 Summary and beam time request

We propose to measure DDVCS on the proton using an 11 GeV electron beam with the SoLIDμ setup in Experimental Hall A at Jefferson Lab. The SoLID spectrometer will be complemented with a forward angle muon detector. The beam spin asymmetry will be measured at a wide range of space-like and timelike virtualities of the incoming and outgoing virtual photons,respectively. It brings novel observables of GPD physics at $x < |\xi|$ which is otherwise inaccessible.

The proposed experiment will run concurrently with the SoLID J/ψ experiment (E12-12-006) approved 60 days (50 production days and 10 calibration days). And we request additional 50 production days beam time to have the total production 100 days. It will use a 11 GeV 3 μA electron beam with polarization (>85%), a 15 cm liquid hydrogen target, and the SoLID spectrometer.

This setup will also complement the statistics of the J/ψ and TCS experiment by detecting the muon channel at the same time. The luminosity during the experiment is planned to be $1.2 \times 10^{37}.cm^{-2}.s^{-1}$. Depending on the background in the detector and SoLID development, the luminosity might be increased to obtain more data.

References

[1] D. Müller, D. Robaschick, B. Geyer, F.M. Dittes, J. Hořejši, Fortschr. Phys. **42** (1994) 101.

[2] X. Ji, Phys. Rev. Lett. **78** (1997) 610.

[3] A.V. Radyushkin, Phys. Rev. **D 56** (1997) 5524.

[4] M. Diehl, Phys. Rep. **388** (2003) 41.

[5] A.V. Belitsky, A. V. Radyushkin, Phys. Rept. **418** (2005) 1.

[6] X.D. Ji, Phys. Rev. D **55** (1997) 7114.

[7] M. Polyakov, Phys. Lett. B **555** (2003) 57.

[8] J.C. Collins, A. Freund, Phys. Rev. D **59** (1999) 074009.

[9] M. Burkardt, Phys. Rev. D **62** (2000) 071503(R).

[10] J.P. Ralston, B. Pire, Phys. Rev. D **66** (2002) 111501(R).

[11] M. Diehl, Eur. Phys. Jour. C **25** (2002) 223.

[12] A.V. Belitsky, D. Müller, Nucl. Phys. A **711** (2002) 118c.

[13] A. Pedrak, B. Pire, L. Szymanowski, J. Wagner, Phys. Rev. D **101** (2020) 114027.

[14] O. Grocholski, B. Pire, P. Sznajder, L. Szymanowski, J. Wagner, Phys. Rev. D **105** (2022) 094025.

[15] M. Guidal, M. Vanderhaeghen, Phys. Rev. Lett. **90** (2003) 012001.

[16] A.V. Belitsky, D. Müller, Phys. Rev. Lett. **90** (2003) 022001.

[17] K. Deja, V. Martinez-Fernandez, B. Pire, P. Sznajder, J. Wagner, Phys. Rev. D **107** (2023) 9.

[18] (CLAS Collaboration) P. Chatagnon *et al.* Phys. Rev. Lett. **127** (2021) 262501.

[19] M. Vanderhaeghen, P.A.M. Guichon, M. Guidal, Phys. Rev. D **60** (1999) 094017.

[20] I.V. Anikin et al., Acta Phys. Pol. B **49** (2018) 741.

[21] A.V. Belitsky, D. Müller, Phys. Rev. D **68** (2003) 116005.

[22] (Hall A DVCS Collaboration) C. Muñoz Camacho *et al.*, Phys. Rev. Lett. **97** (2006) 262002.

[23] (H1 Collaboration) C. Adloff *et al.*, Phys. Lett. B **517** (2001) 47.

[24] (ZEUS Collaboration) S. Chekanov *et al.*, Phys. Lett. B **573** (2003) 46.

[25] (CLAS Collaboration) H.S. Jo *et al.*, Phys. Rev. Lett. **115** (2015) 212003.

[26] (Hall A DVCS Collaboration) M. Defurne *et al.*, Phys. Rev. C **92** (2015) no.5

[27] (Jefferson Lab Hall A Collaboration) F. Georges *et al.*, Phys. Rev. Lett. **128**, 252002

[28] (CLAS Collaboration) N. Hirlinger Saylor et al. , Phys. Rev. C **98**, 045203 (2018).

[29] (COMPASS Collaboration) R. Akhunzyanov *et al.*, Phys. Lett. B **793** (2019) 188; Phys. Lett. B **800** (202) 135129.

[30] (Hall A DVCS Collaboration) M. Mazouz *et al.*, Phys. Rev. Lett. **99**, 242501 (2007).

[31] M. Benali et al., Nat. Phys. **16** (2020) 191.

[32] (HERMES Collaboration) A. Airapetian *et al.*, Phys. Rev. Lett. **87**, 182001 (2001).

[33] (CLAS Collaboration) S. Stepanyan *et al.*, Phys. Rev. Lett. **87**, 182002 (2001).

[34] (CLAS Collaboration) F.X. Girod *et al.*, Phys. Rev. Lett. **100**, 162002 (2008).

[35] (CLAS Collaboration) A. Hobart *et al.*, Phys. Rev. Lett. **133**, 211903 (2024).

[36] (CLAS Collaboration) S. Chen *et al.*, Phys. Rev. Lett. **97**, 072002 (2006).

[37] (HERMES Collaboration) A. Airapetian *et al.*, JHEP **06**, 019 (2010).

[38] (CLAS Collaboration) E. Seder *et al.*, Phys. Rev. Lett. **114**, 032001 (2015).

[39] (CLAS Collaboration) S. Pisano *et al.*, Phys. Rev. D **91**, 052014 (2015).

[40] (HERMES Collaboration) A. Airapetian *et al.*, Phys. Lett. B **704**, 15 (2011).

[41] (HERMES Collaboration) A. Airapetian *et al.*, Phys. Rev. D **75**, 011103 (2007).

[42] (HERMES Collaboration) A. Airapetian *et al.*, JHEP **06**, 066 (2008).

[43] S.V. Goloskokov, P. Kroll, Eur. Phys. J. C **50** (2007) 829.

[44] S.V. Goloskokov, P. Kroll, Eur. Phys. J. C **53** (2008) 367.

[45] M. Burkardt, Int.J. Mod. Phys. A **18** (2003) 173.

[46] H.-W. Lin Phys. Rev. Lett. **127** (2021) 182001.

[47] R. Dupré, M. Guidal, M. Vanderehaeghen, Phys. Rev. D **95** (2017) 011501

[48] C. Lorcé, P. Schweitzer, K. Tezgin, Phys. Rev. D **106** (2022) 014012.

[49] V.D. Burket, L. Elouadrhiri, F.X. Girod, C. Lorcé, P. Schweitzer, Rev. Mod. Phys. **95** (2023) 041002.

[50] E. Voutier, *Nuclear Theory*, Edts. A. Georgieva and N. Minkov, Heron Press, **33**, 142 (2014).

[51] (The Jefferson Lab Positron Working Group) A. Accardi *et al.* Eur. Phys. J. C **57** (2021) 261.

[52] J. Grames *et al.* JaCOW IPAC2023 (2021) MOPL152.

[53] V.D. Burkert, L. Elouadrhiri, F.X. Girod, Nature **557** (2018) 7705.

[54] M. Guidal, Eur. Phys. J. A **37** (2008) 319.

[55] M. Guidal, Phys. Lett. B **689** (2010) 156.

[56] S. Zhao, Ph.D. Thesis, Université Paris-Saclay, Orsay, 2020UPASS147 (2020).

[57] K. Kumerički, D. Müller, K. Passek-Kumerički, Nucl. Phys. B 794 (2008) 244.

[58] H. Moutarde, Phys. Rev. D **79** (2009) 094021.

[59] K. Kumerički, D. Müller, M. Murray, Phys. Part. Nucl. **45** (2014) 723.

[60] K. Kumerički, D. Müller, A. Schäfer, JHEP **07** (2011) 73.

[61] H. Moutarde, P. Sznadjer, J. Wagner, Eur. Phys. J. C **79** (2019) 614.

[62] M. Čuić, K. kumerički, A. Schäfer, Phys. Rev. Lett. **125** (2020) 232005.

[63] V. Bertone, H. Dutrieux, H. Moutarde, P. Sznadjer, Phys. Rev. D **103** (2021) 114019.

[64] Near Threshold Electroproduction of J/ψ at 11 GeV http://www.jlab.org/exp_prog/proposals/12/PR12-12-006.pdf

[65] Timelike Compton Scattering on the proton in e^+e^- pair production with SoLID at 11 GeV https://www.jlab.org/exp_prog/proposals/15/PR12-12-006A.pdf

[66] SoLID Pre-Conceptual Design Report https://solid.jlab.org/DocDB/0002/000282/001/solid-precdr-2019Nov.pdf

[67] Computer Physics Communications 136, 126-147 (2001), https://research.kek.jp/people/tabe/grape

[68] https://github.com/JeffersonLab/evgen_bggen

[69] CLAS12-NOTE-2017-001 (arXiv:1703.08081) and CLAS12-NOTE-2017-014 (arXiv:1712.07712), https://github.com/skorodumina/twopeg

[70] C. A. Aidala *et al.* [SeaQuest], Nucl. Instrum. Meth. A **930**, 49-63 (2019) doi:10.1016/j.nima.2019.03.039 [arXiv:1706.09990 [physics.ins-det]].